

**REPORT DOCUMENTATION PAGE**

*Form Approved  
OMB No. 0704-0188*

Public reporting burden for this collection of information is estimated to average 1 hour per response, including the time for reviewing instructions, searching existing data sources, gathering and maintaining the data needed, and completing and reviewing the collection of information. Send comments regarding this burden estimate or any other aspect of this collection of information, including suggestions for reducing this burden, to Washington Headquarters Services, Directorate for Information Operations and Reports, 1215 Jefferson Davis Highway, Suite 1204, Arlington, VA 22202-4302, and to the Office of Management and Budget, Paperwork Reduction Project (0704-0188), Washington, DC 20503.

<b>1. AGENCY USE ONLY (Leave blank)</b>	<b>2. REPORT DATE</b> 7 Jan. 99	<b>3. REPORT TYPE AND DATES COVERED</b>  THESIS
---	------------------------------------	---

<b>4. TITLE AND SUBTITLE</b> PHYSICAL AND CHEMICAL ALTERATIONS OF ICES BY FAST PROTON IRRADIATION, PARTICULARLY OZONE SYNTHESIS	<b>5. FUNDING NUMBERS</b>
--	---------------------------

<b>6. AUTHOR(S)</b> CAPT ATTEBERRY CHRISTOPHER L	
---	--

<b>7. PERFORMING ORGANIZATION NAME(S) AND ADDRESS(ES)</b> UNIVERSITY OF VIRGINIA	<b>8. PERFORMING ORGANIZATION REPORT NUMBER</b>
---	---

<b>9. SPONSORING/MONITORING AGENCY NAME(S) AND ADDRESS(ES)</b> THE DEPARTMENT OF THE AIR FORCE AFIT/CIA, BLDG 125 2950 P STREET WPAFB OH 45433	<b>10. SPONSORING/MONITORING AGENCY REPORT NUMBER</b>  FY99-2
--	---

<b>11. SUPPLEMENTARY NOTES</b>
--------------------------------

<b>12a. DISTRIBUTION AVAILABILITY STATEMENT</b> Unlimited distribution In Accordance With AFI 35-205/AFIT Sup 1	<b>12b. DISTRIBUTION CODE</b>
---	-------------------------------

<b>13. ABSTRACT (Maximum 200 words)</b>  <div style="text-align: right; font-size: 2em; font-weight: bold;">19990120 033</div>
--

<b>14. SUBJECT TERMS</b>	<b>15. NUMBER OF PAGES</b> 62
	<b>16. PRICE CODE</b>

<b>17. SECURITY CLASSIFICATION OF REPORT</b>	<b>18. SECURITY CLASSIFICATION OF THIS PAGE</b>	<b>19. SECURITY CLASSIFICATION OF ABSTRACT</b>	<b>20. LIMITATION OF ABSTRACT</b>
--	---	--	-----------------------------------

**Physical and Chemical Alterations of Ices by Fast Proton Irradiation,  
Particularly Ozone Synthesis**

---

*A Thesis  
Presented to  
The Faculty of the School of Engineering and Applied Science  
University of Virginia*

---

*In Partial Fulfillment  
Of the requirements for the Degree  
Master of Science in Engineering Physics*

By Christopher L. Atteberry  
January 1999

APPROVAL SHEET

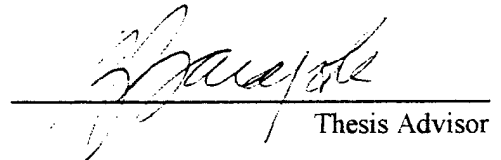
The thesis is submitted in partial fulfillment of the  
Requirements for the degree of

Master of Science in Engineering Physics



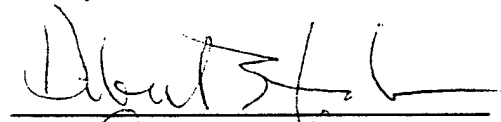
---

The thesis has been read and approved by the examining Committee:

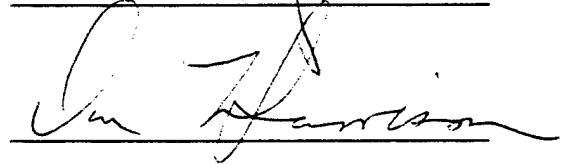


---

Thesis Advisor



---



---

---

Accepted for the School of Engineering and Applied Science:

---

Dean, School of Engineering and  
Applied Science

January 1999

## TABLE OF CONTENTS

Abstract .....	iii
Acknowledgements.....	iv
List of Figures .....	v
List of Symbols and Abbreviations.....	vii
1.0 Introduction .....	1
1.1 Motivation .....	1
1.2 Background .....	2
2.0 Experimental Apparatus and Methods.....	6
2.1 Vacuum Chamber .....	6
2.2 Ion Beam .....	8
2.3 Thin Film Preparation.....	10
2.4 Optical Reflectance.....	14
2.5 Thermally Programmed Desorption (TPD).....	17
2.6 Microscopy.....	20
3.0 Visual Observations of Vapor-Deposited Films .....	22
4.0 Oxygen Formation Experiments—Results and Analysis .....	27
4.1 Reflectance results .....	27
4.2 TPD results .....	29
5.0 Ozone Experiments – Results and Analysis.....	32
5.1 Water Ice Films.....	32
5.2 Oxygen/Water Mixed-Ice Films.....	34
5.3 Other Ices.....	43
5.4 TPD Results for Ozone Experiments.....	50
6.0 Conclusions .....	54

APPENDIX A – Luminescence experiments.....	57
APPENDIX B - Equipment Calibration .....	59
REFERENCES.....	61

## Abstract

In this thesis, we investigated the interaction of 100 keV protons with thin ice films grown under ultra-high vacuum conditions. We determined irradiation of pure water ice produced an *upper limit* of 0.04 O<sub>2</sub>/proton that stayed within the film. Determination of this value came from thermally desorbing the films and measuring the O<sub>2</sub> released with a quadrupole mass spectrometer.

Irradiation of films of solid oxygen, carbon dioxide, hydrogen peroxide, and oxygen/water mixtures led to significant ozone (O<sub>3</sub>) production. We quantified ozone production within the films using thermal desorption and ultraviolet reflectance techniques. Direct irradiation of pure water films did not yield any measurable ozone signal.

We compared our results with recent astronomical observations of icy moons in the outer solar system. Molecular oxygen, created and trapped in water ice by 100 keV proton bombardment, seems insufficient to account for the oxygen absorption features (in the visible spectrum) discovered on Ganymede. Ozone produced from oxygen/water mixed-ice films generates a Hartley band (in the ultraviolet) similar in depth to those seen on Ganymede, Rhea, and Dione. The difference in laboratory band *position* compared with satellite band position suggests the need to revise assumptions concerning the surface ice.

## **Acknowledgements**

My heartfelt thanks to all who made this project possible. Dr. Raul Baragiola, advisor and trusted critic, spent countless hours reviewing my data, answering my questions, and keeping me on course when the route became too convoluted for me to follow alone. The guys in the lab, Tyfo, Dave, and Marcus taught me the ropes and a certain respect for stainless steel vacuum chambers and turbo pumps. Their technical expertise, common sense, and friendship made a great difference in my progress over these past 18 months. Finally (and most of all) my wife, Kim, and daughter, Madelaine, gave me their limitless patience, support, and love. Their influence in my life provided the motivation and enthusiasm I needed to complete my work at the University of Virginia.

## List of Figures

Figure 1: Ganymede/Callisto reflectance ratios, from Calvin and Spencer (1997).....	2
Figure 2: Hartley band on Ganymede, from Noll et al. (1996).....	3
Figure 3: Reflectance ratios for satellites of Saturn, from Noll et al. (1997).....	4
Figure 4: UHV chamber and attached components.....	6
Figure 5: Energy spectrum of Jovian magnetospheric ions, from Ip et al. (1997).....	8
Figure 6: Schematic of reflectance experiments.....	16
Figure 7: Schematic of target assembly.....	20
Figure 8: Calibration grid used to measure microscopic structure.....	21
Figure 9: Proton beam spot on crystalline water ice film.....	22
Figure 10: Low-magnification images of water-ice film growth.....	23
Figure 11: High-magnification images of water-ice film growth.....	23
Figure 12: Low-magnification detail of amorphous water-ice film.....	24
Figure 13: High-magnification detail of amorphous water-ice film.....	24
Figure 14: Ice needles, minimum magnification.....	25
Figure 15: Ice needle, maximum magnification.....	25
Figure 16: Ice needle after irradiation.....	26
Figure 17: Reflectance ratio of irradiated water ice in the visible.....	28
Figure 18: Absorption bands for pure O <sub>2</sub> at various temperatures.....	28
Figure 19: Mass 36 yields from two 20 μm amorphous ice films at 70 K.....	30
Figure 20: Reflectance spectra for H <sub>2</sub> O <sub>2</sub> and irradiated H <sub>2</sub> O.....	33
Figure 21: Typical Hartley band of a 10 μm-thick film showing band depth of 17%.....	35
Figure 22: Low fluence irradiation of a 50 μm-thick CO <sub>2</sub> film.....	36
Figure 23: High fluence irradiation of a 50 μm-thick CO <sub>2</sub> film.....	36



Figure 24: Summary plot of band depth vs. fluence for O <sub>2</sub> :H <sub>2</sub> O films at six temperatures.....	38
Figure 25: Summary plot of absorbance vs. fluence for O <sub>2</sub> :H <sub>2</sub> O films. ....	38
Figure 26: Evolution of the Hartley band in an irradiated film as it was warmed .....	39
Figure 27: Changes in the reflectance of an O <sub>2</sub> :H <sub>2</sub> O film as a function of fluence.....	40
Figure 28: Depiction of background slope.....	41
Figure 29: Slope subtraction procedure. ....	42
Figure 30: Position of the Hartley band minima as a function of fluence and temperature .....	43
Figure 31: Summary plot of absorbance vs. fluence for O <sub>2</sub> , CO <sub>2</sub> , and H <sub>2</sub> O <sub>2</sub> .....	44
Figure 32: Comparison of Hartley bands for various films.....	45
Figure 33: Layered plot comparing laboratory results and astronomical observations .....	47
Figure 34: Layered plot comparing a 50 K O <sub>2</sub> :H <sub>2</sub> O film and solid O <sub>3</sub> .....	48
Figure 35: Ratio subtraction, suggesting the presence of other absorbers at Ganymede.....	49
Figure 36: Thermal desorption: O <sub>3</sub> evolved from an irradiated O <sub>2</sub> :H <sub>2</sub> O film.....	50
Figure 37: Thermal desorption: O <sub>3</sub> evolved from an irradiated H <sub>2</sub> O <sub>2</sub> film.....	51
Figure 38: Thermal desorption: O <sub>3</sub> evolved from an irradiated CO <sub>2</sub> .....	51
Figure 39: Electron-induced luminescence in H <sub>2</sub> O at 77° K, from Merkel and Hamill (1971) ....	57
Figure 40: Luminescence of water ice in the UV .....	58

## List of Symbols and Abbreviations

$\rho$	density
$\tau$	time constant for amorphous $\rightarrow$ crystalline transition
$\lambda$	wavelength
$\sigma$	photoabsorption cross-section
$\Delta f$	change in microbalance frequency
$\Delta m$	change in mass measured by microbalance
$\alpha$	absorption coefficient (exponent in Beer's Law)
A	area of quartz crystal
Å	Ångstrom
CCD	charge coupled device
$F$	fraction of ice remaining amorphous after time $t$
FOS	Faint Object Spectrograph, on Hubble Space Telescope
FWHM	full width at half maximum
HST	Hubble Space Telescope
K	degree Kelvin
keV	kilo electron-volt
kV	kilovolt
lpi	lines per inch
nA	nano-ampere
QCM	quartz crystal microbalance
$R$	reflectance ratio
RGA	residual gas analyzer
s	microbalance constant relating frequency change to mass change

Torr	unit of pressure (760 Torr = 1 atmosphere)
TPD	thermally programmed desorption
UHV	ultra-high vacuum
UV	ultraviolet
UVS	Ultraviolet Spectrometer (on board Galileo)
$\mu\text{m}$	micron

## 1.0 Introduction

### 1.1 Motivation

Recent discoveries show Ganymede, Jupiter's largest moon, maintains unexpected quantities of dense molecular oxygen and ozone [Spencer et al., 1995; Noll et al., 1996]. The findings raise intriguing questions. How did these species originate and why do they remain? Do they regenerate, or are they residual matter from undetermined physical processes? Where exactly do the molecules reside? For instance, different theories suggest the gases are either trapped as inclusions within the icy surface layer, lie frozen upon the surface, or exist as frozen particles in the atmosphere. These questions motivate this research project.

To try to solve some of these mysteries, we devised a series of experiments aimed at duplicating, in the laboratory, conditions around Jupiter and its moons. First, all experiments occurred at ultra-high vacuum (UHV) pressures in a stainless steel chamber evacuated by a cryogenic vacuum pump. UHV pressures approximate the tenuous atmospheres of icy satellites. Second, refrigeration techniques generated low temperatures similar to those of planetary surfaces distant from the sun. Third, a particle accelerator provided energetic ions to simulate the bombardment of surfaces by ions from Jupiter's magnetosphere.

Our experimental apparatus proved useful for studying another water ice property of current interest: radiation-induced luminescence. We conducted luminescence experiments simultaneously with our investigation of the production of ozone and oxygen. Since this topic does not relate directly to the main issue of the thesis, we include the luminescence results in an appendix. We also include optical microscope images of some of our results, providing a visual reference for the topics we discuss.

## 1.2 Background

Ganymede is tidally locked with Jupiter, so one hemisphere always faces the direction of orbital motion, while the opposite hemisphere always faces “backwards”. The trailing hemisphere receives preferential bombardment by ions in Jupiter’s magnetosphere, which rotates more rapidly than the satellite orbits the giant planet. Using data from the Hubble Space Telescope (HST) and ground-based observations of Ganymede, Spencer et al. computed a ratio of the reflectance spectra of Ganymede’s trailing hemisphere to that of Callisto [Spencer et al., 1995, Calvin and Spencer, 1997]. The ratio showed a <2% absorption band at 5770 Å, and a slightly shallower feature at 6275 Å, both on Ganymede’s trailing hemisphere. These two bands (Figure 1) are the result of a weak absorption of a photon by two adjacent oxygen molecules; the features match well with the electronic signature of condensed oxygen [Calvin et al., 1996; Vidal et al., 1997; Baragiola and Bahr, 1998]. The strength of these two bands on Ganymede indicate an optical column density of  $2.6 \times 10^{19} \text{ O}_2/\text{cm}^2$ , corresponding to a 17  $\mu\text{m}$  path length [Vidal et al., 1997].

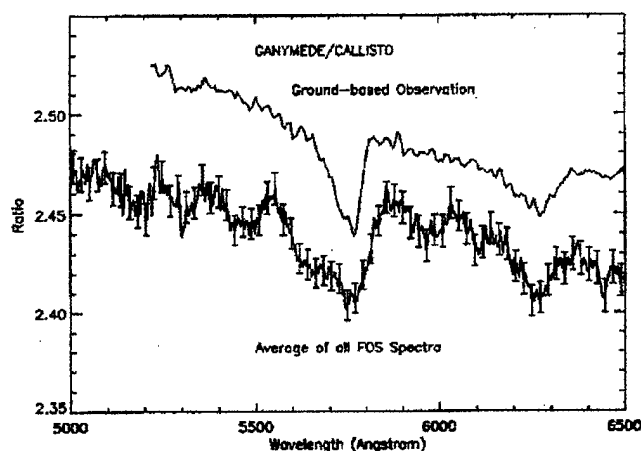


**Figure 1: Ratios of Ganymede/Callisto reflectance for the entire spatial extent of the Faint Object Spectrograph (FOS) of the Hubble Space Telescope, compared with the ground-based spectrum of Spencer et al. (1995) [Calvin and Spencer, 1997].**

Although the latest research has been unable to detect similar bands on any of the other satellites of Jupiter or Saturn [Spencer, 1998], investigators have made another important discovery. On Ganymede, Rhea, and Dione (the latter two in Saturn's system), ultraviolet measurements have revealed the presence of ozone [Noll et al., 1997]. The detection of ozone on icy bodies leads to the real possibility of molecular oxygen being present as well. For instance, it is the gaseous oxygen in Earth's atmosphere that accounts for the production of ozone; the two molecules are intimately related. Ozone can signal the presence of  $O_2$  efficiently, since only a small column density of ozone (equivalent to a few molecular monolayers) is required to generate an observable band in the ultraviolet.

The ozone feature in the ultraviolet region, known as the Hartley band, is a much broader absorption than the visible band due to condensed  $O_2$ . Figure 2 shows the Hartley band discovered on Ganymede.

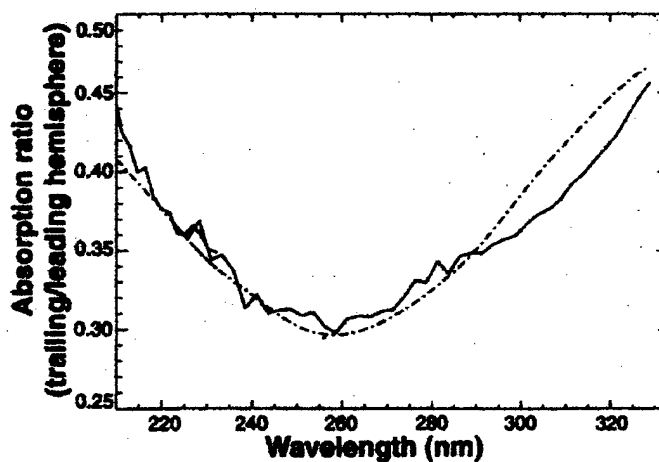


Figure 2: Hartley band on Ganymede. The dashed line is a model spectrum based on an ozone column abundance of  $4.5 \times 10^{16} O_3/cm^2$  [Noll et al., 1996].

The band was discovered by dividing the spectrum of the trailing hemisphere by that of the leading hemisphere. In Ganymede's case, the band is ~30% deep, corresponding to  $4.5 \times 10^{16} \text{ O}_3/\text{cm}^2$  [Noll et al., 1996]. The  $\text{O}_3$  column density is about a thousand times smaller than the value for  $\text{O}_2$  in the same hemisphere, yet the  $\text{O}_3$  band depth is approximately 15 times greater.

On the Saturnian satellites, the ozone absorption features are weaker (less than 8%), but still easily discernible. Figure 3 gives the spectra for Rhea and Dione, where the absorption features seem to be superimposed on a background slope, a feature we will discuss in some detail in this thesis.

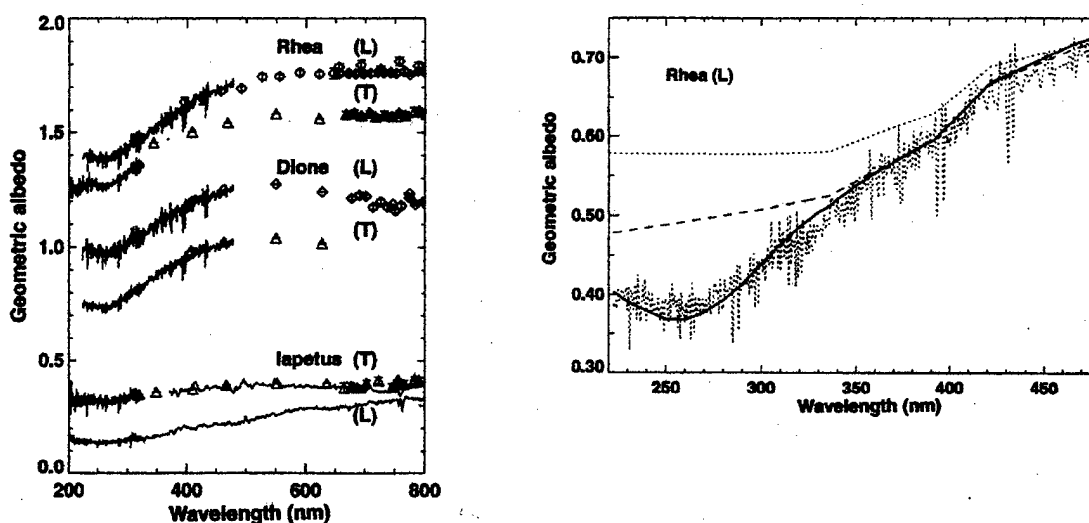


Figure 3: Reflectance ratios for satellites of Saturn. The graph on the left depicts the hemispheric geometric albedos of Rhea, Dione and Iapetus. The authors vertically offset the curves for clarity. Notice the Iapetus spectra seem to have a weak minima, but at different wavelength than Rhea and Dione. The graph on the right depicts a model including  $\text{O}_3$  (solid line), plotted with the spectrum of Rhea's leading hemisphere [Noll et al., 1997].

Using these discoveries as a starting point, we attempted to better understand these phenomena through laboratory experiments. We bombarded cold, thin ice films with energetic ions to see if we could produce oxygen and ozone molecules that would remain in the ice. We employed reflectance techniques similar to those used in the astronomical studies, reflectance

ratios being the centerpiece of our investigations. The interesting results from these studies will be reported in the body of this thesis.



## 2.0 Experimental Apparatus and Methods

### 2.1 Vacuum Chamber

We begin by describing the heart of the experiments: the UHV chamber. In Figure 4, we indicate the most important components of the apparatus.

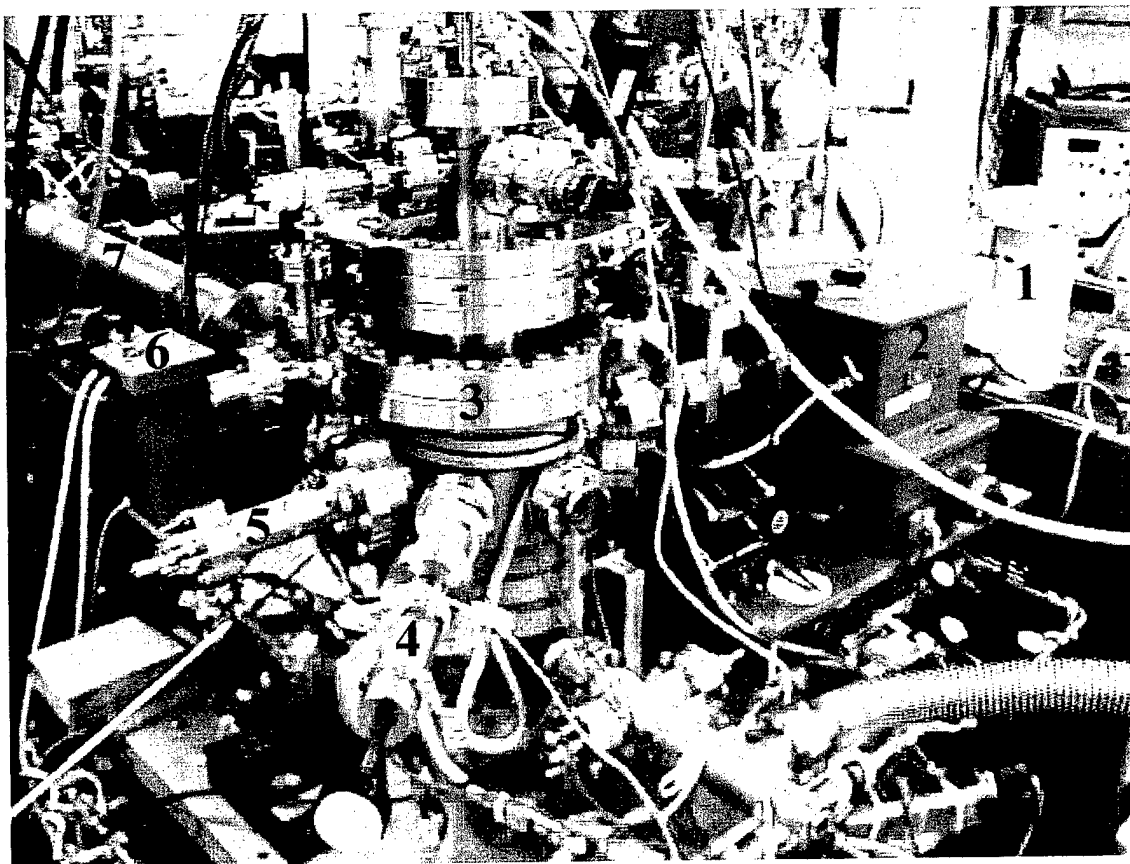


Figure 4: UHV chamber and attached components.

1. Liquid nitrogen dewar for optical spectrometer
2. Optical spectrometer
3. Ultra-high vacuum chamber
4. Retractable doser
5. Mass spectrometer
6. Light source
7. Beam line

A CTI-Cryogenics Cryo-Torr 7 pump attached to the bottom of the chamber maintained vacuum in the  $10^{-9}$  Torr range; we determined chamber pressures with a Bayard-Alpert ionization gauge. Multiple ports allowed access to the body of the chamber, providing the means to grow thin films on a centered target, irradiate the films with energetic ions, and quantitatively measure their properties under a variety of circumstances. For example, one port was dedicated to a quadrupole mass spectrometer, while another permitted light reflected from the target to enter a visible/ultraviolet optical spectrometer. Several quartz windows enabled visual observations, allowing us to image the target with a high magnification, long-distance microscope. The photographic images in this thesis came from an electronic camera attached to this microscope.

The target substrate was the gold electrode of a quartz crystal microbalance (QCM), a piezoelectric device which allowed precise mass measurements during our experiments. The quartz crystal oscillated at its resonant frequency when driven by an external circuit; a change in this frequency was directly proportional to mass change on films deposited on the gold surface [Westley, 1994]. A second crystal on the back of the target (and consequently unexposed to gas deposition) operated in heterodyne with the first, enabling the experimenter to correct for frequency change due to temperature variations. The target assembly was connected to a "cold finger", capable of cooling down to 25 K using a closed-cycle refrigerator (CTI-Cryogenics), or down to 5 K with a liquid helium cryostat. A silicon diode and electrical resistor mounted within the target assembly provided temperature measurement and control, respectively. Finally, the target assembly could be rotated 360 degrees around the vertical, allowing the target to face any of the ports.

## 2.2 Ion Beam

A 300-kilovolt ion implanter, built by Accelerators Inc., generated the ion flux we needed to simulate irradiation at Ganymede. We substituted the high-voltage power supply for the implanter with a newer, solid-state supply (Spellman SL 30) allowing precise voltage control during experiments. In all trials, we used an acceleration voltage to 100 kV; protons of this energy are representative of the distribution of energies in Jupiter's magnetosphere, as shown in Figure 5 below [Ip et al, 1997].

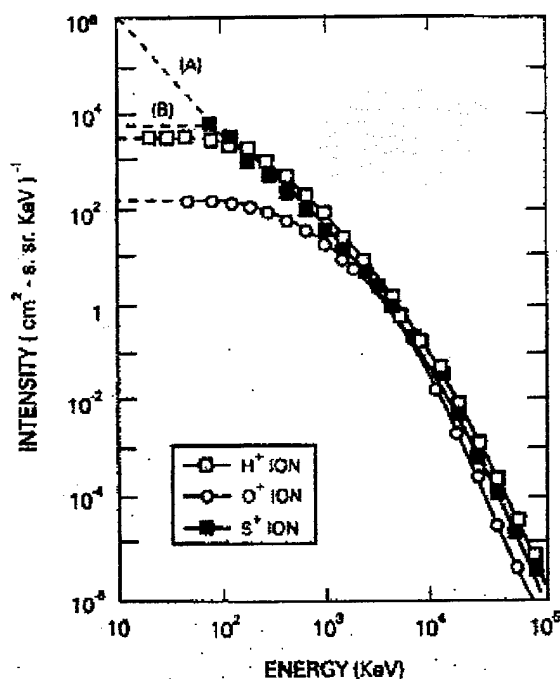


**Figure 5:** An energy spectrum of the Jovian magnetospheric ions from the Energetic Particle Detector (EPD) experiment on Galileo. Data taken at a radial distance of 15 Jupiter radii [Ip et al., 1997].

We also chose protons as our bombarding ion species to achieve a relatively deep ( $\sim 2$   $\mu\text{m}$ ) alteration of the target. To create a proton beam, we introduced research-grade hydrogen gas

into the ion source through a leak valve, where radio frequency oscillators created a plasma. The ion beam, extracted by a 10 kV (maximum) probe voltage, was accelerated by a constant field stage and passed through a mass-separating electromagnet, which bent the ion beam 30 degrees. At the entry point to the chamber, a Faraday cup collected the beam current, which was measured by a Keithley 610C electrometer. By opening the 0.5 cm diameter cup (using a spring-loaded, electromagnetic toggle switch), we allowed a collimated beam of known current to enter the chamber and strike the target. We measured a beam spot of  $0.41 \text{ cm}^2$  (at  $45^\circ$  incidence) on the film with our long-distance microscope. Initially, we connected the target to another electrometer, to ensure the desired current reached its destination. Convinced the chamber was aligned properly, we simply grounded the target in all future experiments to avoid charging effects.

During our investigations, we irradiated films with proton currents from 50 nA to  $2 \mu\text{A}$ , up to total fluences of  $\sim 3 \times 10^{16}$  protons/ $\text{cm}^2$ . Often, the irradiation was accomplished in steps. If we wanted to bombard a film for a certain amount of time, we simultaneously started a stopwatch and opened the Faraday cup. For the shortest irradiations, timed for one second, we estimated an error of 50% in our fluence calculations. Transient fluctuations in the beam current accounted for half of this error, while the inherent inaccuracy of human reflexes added the other half. Our next shortest irradiation period was five seconds, with an estimated error of 20%; current fluctuations caused most of this error, while reflexes accounted for about 6%. As irradiation times increased to 15 seconds and beyond, the current fluctuations averaged out and total error is estimated to be  $\pm 4\%$ .

We varied proton current across experiments to see if any phenomena were current dependent. We were concerned with the possibility of current dependence since our laboratory ion fluxes were high relative to those on Ganymede and other Galilean moons. We were forced the use high currents to keep the length of experiments down to a reasonable time period. Interestingly, the processes occurring on Ganymede's surface appear to have a "limited" time span

as well. The top 10  $\mu\text{m}$  of the surface of Ganymede is expected to be renewed over a period on the order of one hundred years [Spencer, 1987]. This renewal, called "gardening", results from micro-meteorite impacts and consequently limits the total ion fluence at the satellite's surface. In the span of a hundred years, at a flux of  $\sim 2 \times 10^6$  ions/sec/cm<sup>2</sup> [Ip et al., 1997], the surface of Ganymede is irradiated by a proton fluence of  $\sim 6 \times 10^{15}$ /cm<sup>2</sup>. Our goal was to reproduce this total fluence; at 150 nA current, we achieved that goal in about an hour of accelerator operation.

### 2.3 Thin Film Preparation

Experiments started with a thin, vapor-deposited film, composed of either pure water or an oxygen-water mixture, and ranging in thickness from hundreds of nanometers to hundreds of microns. We also made films of O<sub>2</sub>, CO<sub>2</sub> and H<sub>2</sub>O<sub>2</sub> for comparison with the oxygen-water mixtures. Target temperatures were appropriately low enough to ensure nearly complete sticking of the gases onto the gold substrate. We controlled film growth rates during all the experiments very finely using a Granville-Phillips leak valve.

To grow a film, we introduced gas or vapor into a continuously-baked stainless-steel manifold, with a total volume of 1200 cm<sup>3</sup>. An MKS Baratron capacitance manometer (model 222B) measured the pressure inside the manifold, typically 15-25 Torr. The manifold was pumped by a turbo pump to a base pressure of <1 mTorr. Multiple gases (oxygen and water, for example) could be mixed in the manifold, passed through the leak valve to a gas doser mounted to a chamber port, then through a micro-capillary array (Galileo C26S10M50; thickness: 0.5 mm; hole diameter: 50  $\mu\text{m}$ ; hole separation: 120  $\mu\text{m}$ ) into the UHV chamber. We positioned the end of the doser about a millimeter from the target during film growth.

Determining film thickness was challenging, because a quartz crystal micro-balance remains accurate only to a film thickness of about 3  $\mu\text{m}$ . Our optical absorption experiments

often required films 10  $\mu\text{m}$  or greater, to ensure a sufficiently long path length for optical absorption. Therefore, we needed a method other than the QCM to determine thickness. Our solution was to find a relation between the decrease of gas pressure in the manifold and mass deposited on the target. First, we leaked small quantities of oxygen or water onto a bare target, maintaining a thickness within the working range of the QCM. Next, by comparing the decrease in gas pressure in the manifold to the change in crystal frequency, we calculated a relation and extrapolated the equation for use with “thick” films. The fundamental equation for the QCM is:

$$\Delta m = \Delta f \cdot s \cdot A$$

where  $\Delta m$  is the mass change in g,  $\Delta f$  is the frequency change in Hz,  $A$  is the area of the sensitive part of the crystal, and  $s$  is a constant with value  $1.227 \times 10^{-8} \text{ g/Hz} \cdot \text{cm}^2$  for the crystals used in these measurements [Westley, 1994]. To convert this information to film thickness “ $d$ ”, we used:

$$d = \frac{\Delta m}{\rho \cdot A} = \frac{\Delta f \cdot s}{\rho},$$

where  $\rho$  is the density of the material being deposited (water ice:  $0.8 \text{ g/cm}^3$  [Westley et al., 1998]; oxygen:  $1.43 \text{ g/cm}^3$ ). We found a decrease of 1 Torr of water vapor pressure in the manifold resulted in a  $4.5 \mu\text{m}$ -thick film; one Torr of oxygen grew a  $2.5 \mu\text{m}$ -thick film. When we grew oxygen/water mixture films, we used the mean of these two numbers.

Our water ice films ranged in thickness from 500 nm to 100  $\mu\text{m}$  and were grown at temperatures in the range 20 K to 150 K. We varied film thickness to ensure a sufficient photon path length. Since the oxygen absorption features (at 5770  $\text{\AA}$  and 6275  $\text{\AA}$ ) are caused by double

electronic transitions in two adjacent oxygen molecules, one needs sufficient oxygen density and a sufficient photon path length to see the bands. We used different temperature for two reasons. First, the actual surface ice temperature of Ganymede is unknown. The dark material on the surface has a reported daily temperature in the range 90-152 K [Orton et al., 1996]; however, the high albedo of the icy surfaces could result in temperatures much lower in partially shielded, high-slope terrain. Our experiments covered the range of reasonable temperatures for icy moons in the outer solar system.

The second reason for varying film temperature was an attempt to quantify the gas-holding capabilities of different types of ice. Based on the possible range of temperatures on Ganymede, two different phases of ice are likely: amorphous and cubic crystalline. It is well known that water ice grown at temperatures below ~140 K forms a mostly amorphous structure [Sack and Baragiola, 1993], while it assumes a crystalline structure if grown at higher temperatures. Since it appears possible that the icy surfaces of Ganymede and other satellites exist below the transformation temperature, then water ice could grow in the amorphous phase.

Amorphous ice has a significant ability to trap gases [Laufer et al., 1987; Vidal et al., 1997], a property which interested us in our efforts to produce oxygen by proton bombardment. Amorphous ice also transforms spontaneously to cubic ice at temperatures below the transition temperature, according to:

$$F = \exp\left(\frac{-t}{\tau}\right),$$

with  $\tau = 1.13 \times 10^{-13} \exp(5100/T)$ , and F as the fraction of amorphous ice remaining after time t (seconds) in a film at temperature T in Kelvin [Sack and Baragiola, 1993]. If we assume an ice temperature of 121 K, the midpoint of the temperature range 90 K-152 K, then it would take about two days for an amorphous sample to become 50% cubic. However, as mentioned above, the reported temperature is for the dark terrain, and it should be tens of degrees lower for ice due

to its high albedo. If the temperature is 100 K, the time increases to about 37 years; for 90 K, the time is about 10,000 years, one hundred times longer than the “gardening” period already mentioned. In addition, ion irradiation may amorphize crystalline ice [Struzzola et al., 1992]. From this discussion, we cannot rule out either type of ice being present on Jupiter’s satellites. Consequently, it was necessary to grow both types of ice films.

For our oxygen/water films, used during ozone experiments, we added research purity oxygen to water vapor in the manifold, creating a 1:1 mixture measured by partial pressures. Oxygen sublimates strongly at temperature  $>30$  K (vapor pressure  $>10^{-7}$  Torr). Thus, films grown and maintained above that temperature suffered a decline in oxygen concentration over the lifetime of the experiments (generally three hours); we detected this loss directly using the mass spectrometer (see Section 2.5 below). Experiments conducted by Baragiola and Bahr (1998) confirmed that amorphous ice is unable to retain oxygen indefinitely when the films are grown by co-deposition. Without any means of putting oxygen back into the films, our warmer films would eventually exhaust their included oxygen. Consequently, we did not attempt to grow any films above 50 K because of the rapid outgassing of oxygen.

The reader may argue that temperatures of 50 K and below are unlikely for the satellites we were studying. Baragiola and Bahr show, however, that the shape and position of the oxygen bands seen on Ganymede more closely resemble solid oxygen than liquid or gaseous oxygen trapped in bubbles in the ice. Solid oxygen in equilibrium would *have* to exist below 55 K. Since no measurements have been made of just the brightest icy parts of the satellite’s surface, we assumed the low temperatures are possible.

The oxygen/water mixtures appeared translucent, milky white, and smooth. To increase the reflected light in our experiments, we grew each 10  $\mu\text{m}$ -thick film on top of a sub-layer of bright, white amorphous ice. To ensure reproducibility, we grew these substrate water layers 50  $\mu\text{m}$  thick at 85 K. Besides increasing our signal, the water substrate added “realism” to our



experiment. If oxygen on Ganymede is trapped in the ice or condensed on the surface, either way it resides on top of a much thicker water ice layer, leading to the same sort of layered film we grew in the laboratory.

## 2.4 Optical Reflectance

Our investigations of solar system ices centered around reflectance experiments. The reflectance spectrum of a given material in the ultraviolet, visible, and infrared provides information about the properties of the material in a non-destructive way. Reflectance properties play an important role in "remote sensing", where an investigator can collect data from extremely distant locations. Recent studies of Ganymede, Callisto, and other icy moons have used reflectance measurements, with the sun as the light source, to determine the presence of various molecules and atoms on the surface of the satellites [Spencer and Calvin, 1995; Noll et al., 1996; McCord et al., 1997]. We followed the procedures of these investigators in our laboratory experiments, calculating reflectance *ratios* from our raw data. We report these ratios throughout the thesis.

We now discuss the equipment and methods employed in our reflectance experiments. For visible light and UV reflectance experiments, we employed an Acton Research VM 502 vacuum spectrometer with two different diffraction gratings. One grating (with 1200 lines-per-inch) covered the range 1000-5400 Å, the other (with 600 lpi) diffracted light from 4000 to 11,000 Å. A cryogenic pump and an ion pump operated continuously upon the spectrometer assembly; however, since the spectrometer was sealed with Viton gaskets, its lowest possible pressure was on the order of  $10^{-8}$  Torr. To minimize the impact of this relatively high pressure, we isolated the spectrometer from the vacuum chamber with a metal-sealed gate valve when the spectrometer was not in use.

Initially, we needed to calibrate the spectrometer. Originally, the device was designed to work as a monochromator, using an exit slit to select only a single wavelength from the diffracted light, which was then detected by a photomultiplier. To increase the sensitivity of the instrument, we had Acton Research build an adapter to allow the entire diffracted beam to reach a Photometrics SDS 9000 charge-couple device (CCD) detector. The CCD, cooled by liquid nitrogen, was coated with a metachrome film which allowed the device to detect light signals from the ultraviolet through the infrared. Using the 600 lpi grating for light in the visible spectrum, the CCD could capture a spectrum 1461 Å wide, giving a dispersion of 1.43 Å/pixel. We used an Oriel krypton calibration lamp to determine the pixel position corresponding to known wavelengths, and employed a polynomial fit to map wavelength versus pixel across the width of the CCD (see Appendix A for details). Using an identical procedure with an Oriel Hg(Ar) lamp, we calibrated the 1200 lpi grating in the ultraviolet and determined a dispersion of 0.75 Å/pixel.

The choice of light source was an important consideration in reflectance experiments. Our goal was to find a bright source with a “smooth” spectrum over the wavelengths under investigation. Since we were to search for oxygen in the 5500-6500 Å range, a quartz-halogen light source proved the best choice. We verified the smoothness of the quartz-halogen spectrum by reflecting the light from various white substrates, including teflon and BaSO<sub>4</sub>, a reflectance standard in photometric applications. In the ozone experiments, we were interested in wavelengths between 2000-3000 Å. The light source with the smoothest spectrum was an Osram xenon gas-discharge lamp, controlled by an Oriel power supply.

The source lamps were given at least 30 minutes to warm up and stabilize before each experiment, ensuring a constant intensity. The quartz lamp was not adjusted; it was either on or off. The xenon lamp was adjusted to operate at 5.4 amps, the ideal current according to manufacturer specifications. Light from either lamp reflected off a half-silvered mirror, passed

through the collimating Faraday cup opening, and shined onto the target (refer to Figure 6 below).

Because the light and the protons were collimated by the same small opening into the chamber, we were assured the two beams struck the same spot on the target.

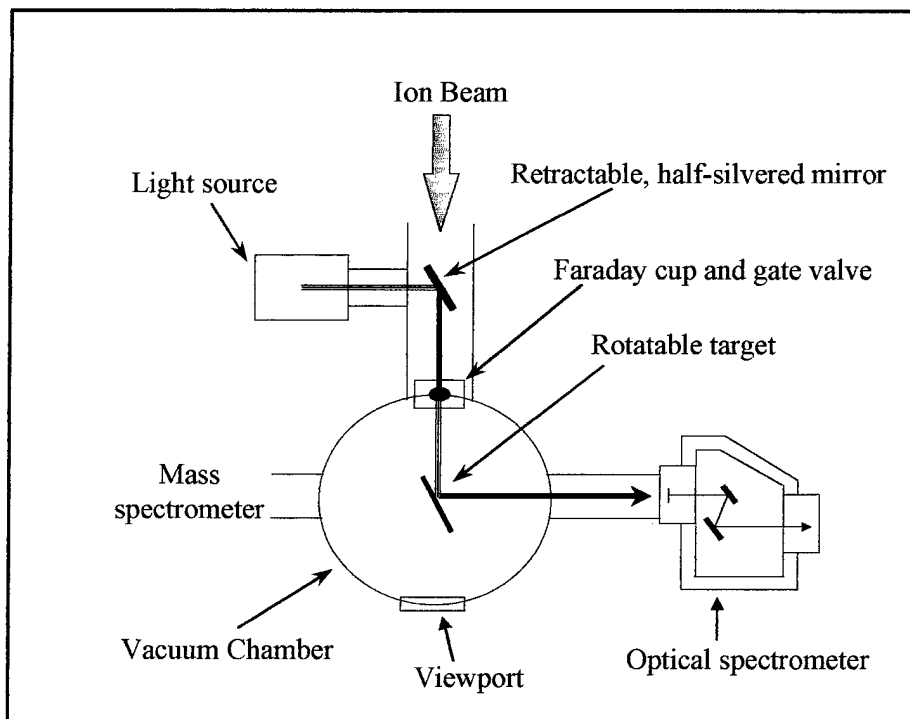


**Figure 6: Schematic of reflectance experiments.**

In reflectance trials, incident light reflected off the target and passed through a bellows connecting the UHV chamber to the spectrometer. Within the bellows we mounted a UV-transparent MgF lens that focused the light on the entrance slit of the spectrometer, enhancing the collection of low-intensity scattered light. After the entrance slit, the light was diffracted by the spectrometer's grating onto the CCD detector. In reflectance experiments, we used CCD exposure times between ten seconds and one minute, depending on the scattering properties of the film under investigation. For the luminescence experiments, we allowed the CCD to operate for up to ten minutes per exposure, since we were searching for very faint signals.

Just as Spencer et al. used spectral data from Callisto as a reference for the trailing hemisphere of Ganymede, we acquired reference spectra for each trial. Our reference spectra

were simply CCD exposures of the light source reflected from the unbombarded target film. For each experiment, we obtained a "dark" spectrum by shutting off the incident light beam with the gate valve between the vacuum chamber and the accelerator beam line. This dark spectrum, subtracted from subsequent measurements, corrected for the significant noise and electronic bias produced by the CCD detector. Because the CCD array could only cover a limited spectral range with each exposure, we acquired spectra centered at regularly spaced intervals. For instance, in the ozone studies, we covered the wavelengths from 2000-3200 Å by measuring reflected light centered at 2300 Å, 2600 Å, and 2900 Å. We took measurements at each of these intervals *before* and *after* irradiation, ensuring each data set would match with its own reference. The reflectance ratio is given by:  $R = (\text{Irradiated} - \text{Dark}) / (\text{Reference} - \text{Dark})$ .

Finally, by intentionally overlapping the edges of the individual spectra, we could gather a coherent picture for our complete wavelength range. Using overlapping pictures helped corroborate data, since an absorption feature that appeared in multiple spectra was more convincing than a single occurrence in one CCD image.

## **2.5 Thermally Programmed Desorption (TPD)**

Since our films were not significantly damaged during reflectance trials, we could further analyze the compositions with a follow-on desorption experiment. Thermal desorption experiments used an Ametek LC Series quadrupole mass spectrometer. Known as a Residual Gas Analyzer (RGA), it passed its data directly to the same computer as the CCD. The RGA sampled the species in the chamber according to their mass, allowing an accurate compositional analysis of sublimating thin films. The RGA displayed partial gas pressures of each specie as a function of time, while we used a separate computer program to record the temperature. Film temperatures were controlled automatically using a Lakeshore 330 controller, or manually when we employed

liquid helium as the refrigerant. In many cases, when we were interested only in the total desorbed quantity of a particular gas (without any reference to temperature), we simply detached the cold finger from the refrigerant, and allowed the target to warm up.

In our TPD experiments, we looked specifically for the quantity of O<sub>2</sub> and O<sub>3</sub> contained within ice films after proton irradiation. These quantities could then be used as supporting evidence for data collected in reflectance experiments. For instance, if we detected an ozone absorption band with UV light, we expected to find a corresponding number of ozone molecules during desorption of the film. Ultimately, we hoped to find the O<sub>2</sub> and O<sub>3</sub> yields per incident proton. Since the RGA is used to measure pressures in the vacuum chamber, and we needed molecular quantities instead, we had to calibrate the flux of molecules desorbing from the target in terms of the partial pressure.

We returned to the quartz crystal micro-balance as a calibration instrument. The O<sub>2</sub> calculation was accomplished with the research-grade oxygen we used in our film growth. By condensing a known mass of O<sub>2</sub> on the target, then sublimating that film, we could relate the number of molecules leaving the target (calculated from the mass loss measured with the QCM) to the partial pressure of the gas in the chamber. We found the following relationship between the integral  $\int P dt$  of the desorbed O<sub>2</sub>, and the number of oxygen molecules per square centimeter desorbed from the target over the duration of the experiment. For oxygen (not valid for other gases) [D. Bahr, personal communication]:

$$1 \text{ Torr} \cdot \text{sec} = (1.0 \pm 0.5) \times 10^{22} \text{ molecules O}_2 / \text{cm}^2 .$$

Since we did not have a dedicated O<sub>3</sub> source, we determined the ozone calibration based on the number we found for oxygen. An RGA has a sensitivity factor for every gas, and this factor is approximately equal for O<sub>2</sub> and O<sub>3</sub> [Siegel, 1982]. This equivalence allowed us to use the same calibration value for ozone as for oxygen. With this single calibration factor, we could

determine the yield per proton (for both O<sub>2</sub> and O<sub>3</sub>) by dividing our integrated TPD results (given in units of molec/cm<sup>2</sup>) by ion fluence.

Thermal isolation of the target is an important consideration in the desorption experiments. Since the target sample was attached to the end of a stainless steel tube, thermal contact with the outside world passed primarily along this route. We wanted to ensure the target temperature was the lowest of all the surfaces in the chamber. In other words, the temperature had to decrease as one moved down the cold finger to the target. If not, gases sublimating from the target could condense on colder surfaces elsewhere, instead of being detected by the RGA. As the entire system continued to warm, these other surface would release their gas loads, and the RGA would measure gas that had already left the target at an earlier time and temperature. To minimize this problem, we added a second temperature measuring diode and heater element higher up the cold finger, allowing us to monitor and maintain the cold finger at a temperature above that of the target (see Figure 7 below).

The target could also receive energy through thermal radiation from the vacuum chamber walls. During the liquid helium experiments, radiation flux was inconsequential because of the high cooling efficiency of helium. However, radiation effects were important when we used the closed-cycle refrigerator. During our initial experiments with this refrigerator, the target was surrounded by two heat shields. Unfortunately, the shields also adsorbed unknown quantities of molecules desorbing from the target, making the sublimation data difficult to analyze. When we removed the shields, the refrigerator was unable to lower the target temperature below about 50 K. At this point, we switched to the liquid helium cryostat. We note that an open geometry (no shields) was also used by Vidal et al. (1997) and Baragiola and Bahr (1998) in their studies of oxygen-trapping in ice in our laboratory.

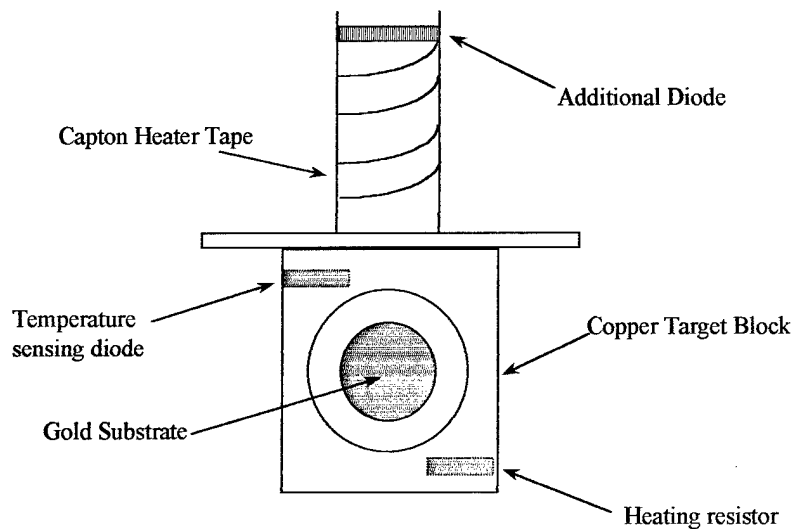


**Figure 7: Schematic of target assembly.**

## 2.6 Microscopy

To “see” the changes occurring in ice films during their growth, as well as their evolution resulting from proton irradiation, we used a long-distance microscope assembly (Optem model Zoom 70) to image the target. Previous researchers [Laufer et al., 1987] acquired pictures of amorphous ice films that showed interesting microstructures referred to as “ice needles”. We captured these structures at maximum magnification with a Pixera CCD camera (model PVC 100C) attached to the microscope. Since the focal length of the lens was fixed, we had ISI manufacture a special “re-entrant” style window for the vacuum chamber. This window, attached to the end of a hollow cylinder that protruded into the chamber, enabled us to place the lens within 9 cm of the target. We illuminated the films with a focused halogen light mounted to a port 45° from the re-entrant window.

We determined the dimensions of objects in our CCD images by calibrating the lens with a fine-mesh nickel screen, shown in Figure 8 below. Spacing between wires was 25  $\mu\text{m}$ , allowing us to determine a resolution of approximately 3  $\mu\text{m}$ .

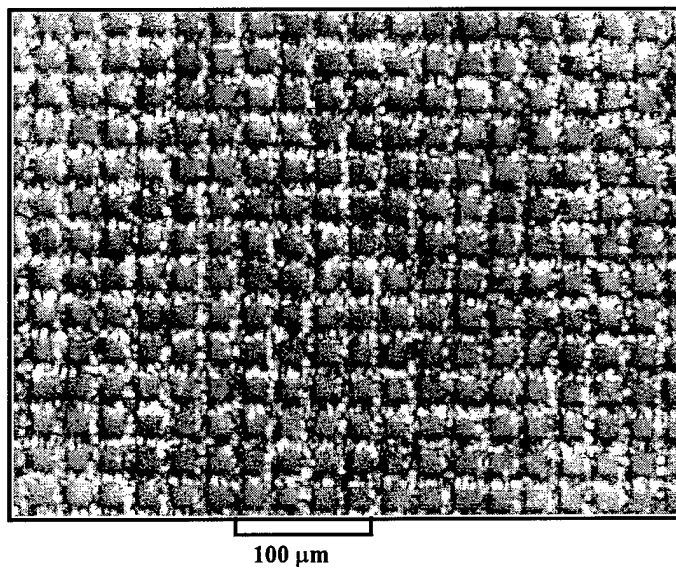


**Figure 8: Calibration grid used to measure microscopic structure.**



### 3.0 Visual Observations of Vapor-Deposited Films

We present our observations on vapor-deposited water ice films grown under UHV conditions. Water ice films deposited above  $\sim 130$  K were transparent, even at thicknesses of 50-100  $\mu\text{m}$ . Films grown below  $\sim 120$  K were opaque, white, and rough in texture. Note the first temperature range corresponds to crystalline ice, while the second range to amorphous ice. Transparent films were difficult to image until they had been irradiated. After irradiation, the area affected by the beam was remarkably changed. The smooth, clear surface of the crystalline ice was replaced with a frosty, fractured texture that was easily photographed. A similar observation was reported by Brown et al. (1978) in their investigation of sputtering of ice by MeV light ions. Figure 9 is an image of a 20  $\mu\text{m}$ -thick crystalline film after bombardment ( $1 \times 10^{16}$  protons/ $\text{cm}^2$ ) at 120 K, showing the distinct boundary between irradiated and unirradiated ice.

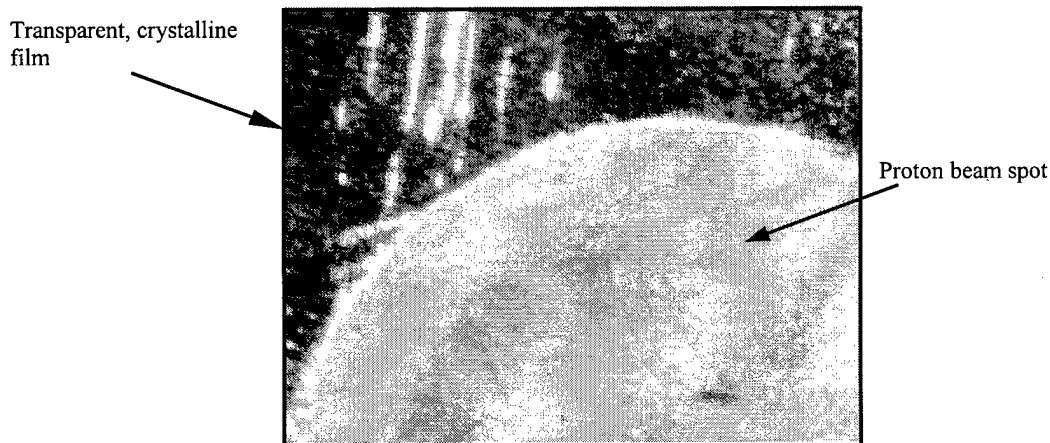


**Figure 9: Proton beam spot on crystalline water ice film.**

In the following series of images (Figure 10 and 11), we capture film growth of an amorphous water ice film at 60 K. The target was angled  $45^\circ$  to the lens.

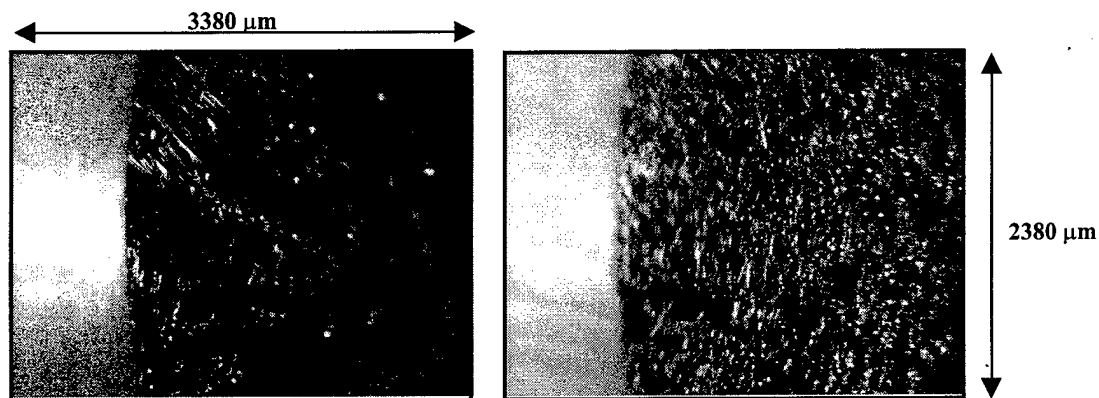


**Figure 10:** Time lapse photograph of a water ice film condensing on the target, imaged at minimum magnification. Developing grains are visible on the highly polished gold substrate (dark portion in the pictures). Film thicknesses were  $1.3 \mu\text{m}$  and  $3.3 \mu\text{m}$  for the left and right pictures, respectively.

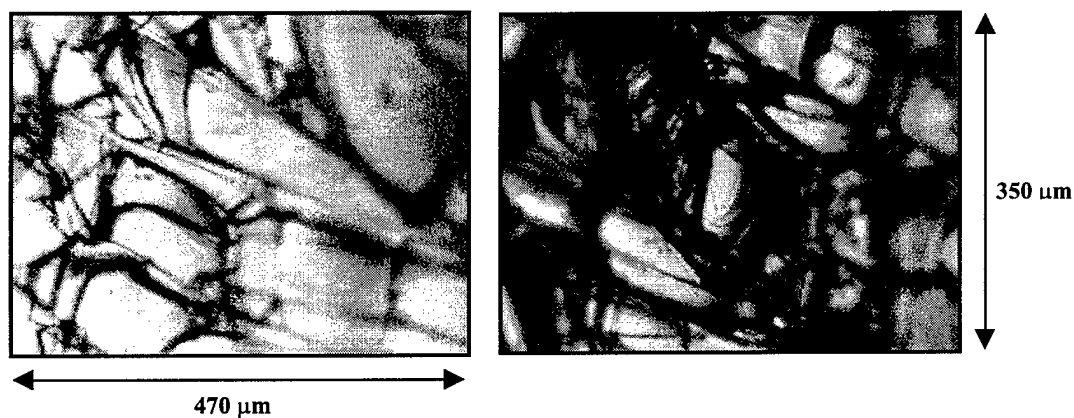


**Figure 11:** Two images at maximum magnification, further along in growth. Film thicknesses were  $11 \mu\text{m}$  and  $21 \mu\text{m}$  for the left and right pictures, respectively.

After film growth was complete ( $50 \mu\text{m}$  thick,  $60 \text{ K}$ ), we rotated the target to various angles, highlighting the grain structure and ice needles. Figures 12 and 13 show different magnifications at normal incidence with an illumination phase angle of  $45^\circ$ .

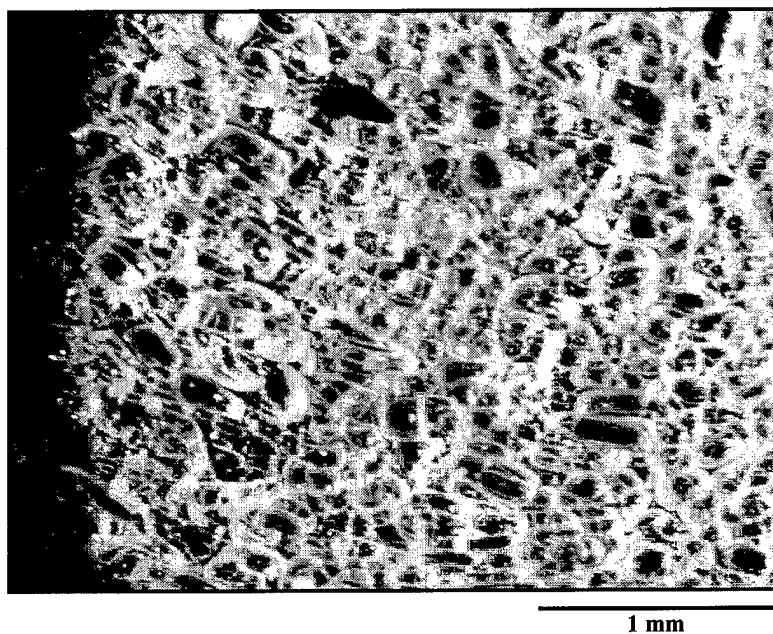


**Figure 12:** Amorphous water ice film 50  $\mu\text{m}$  thick (minimum magnification). The image size is 3380 x 2380  $\mu\text{m}$ .

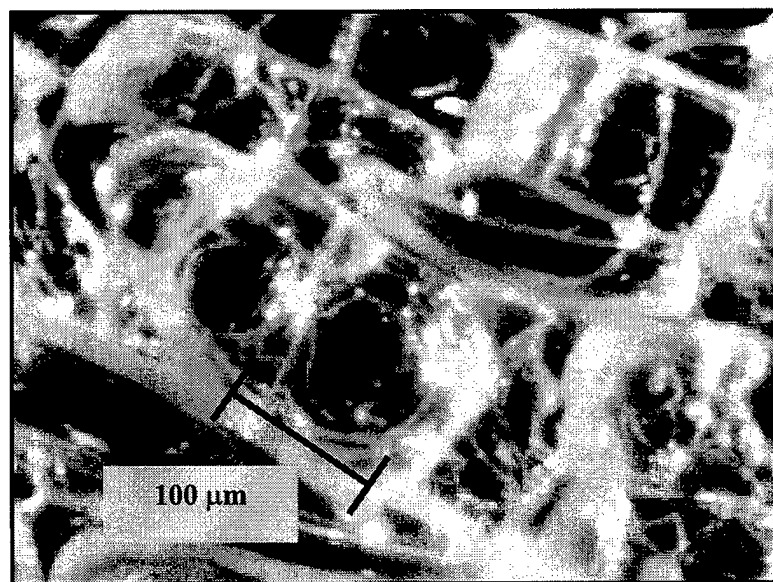


**Figure 13:** Amorphous water ice film, 50  $\mu\text{m}$  thick (maximum magnification). The image size is 470 x 350  $\mu\text{m}$ .

Figures 14 and 15 depict the ice needle structure seen by previous researchers [Laufer et al,1987]. For these picture, the target was rotated so that the surface was at  $20^\circ$  with respect to the lens axis.

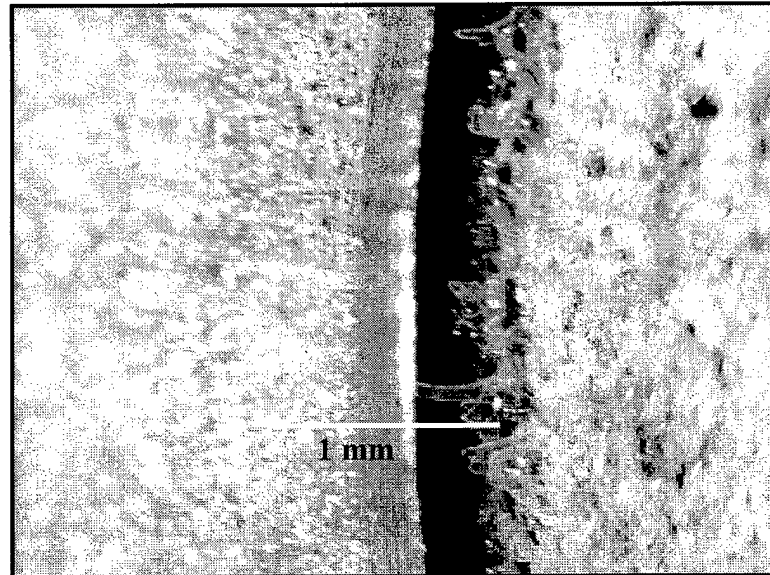


**Figure 14: Ice needles, minimum magnification, 50  $\mu\text{m}$ -thick water ice. The image size is 3380 X 2380  $\mu\text{m}$ .**

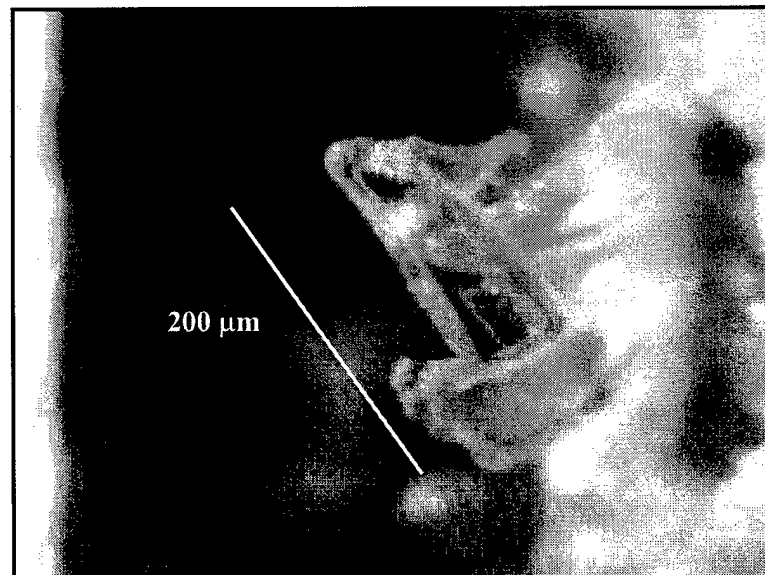


**Figure 15: Ice needle, maximum magnification, 50  $\mu\text{m}$ -thick water ice. The image size is 470 x 350  $\mu\text{m}$ .**

In the final image (Figure 16), we show the same ice needle region after proton bombardment with  $8.8 \times 10^{15}$  protons/cm<sup>2</sup>. Notice that the crisp ice structure seen in Figure 15 now looks “melted” or eroded, like old snow in a parking lot after several days.

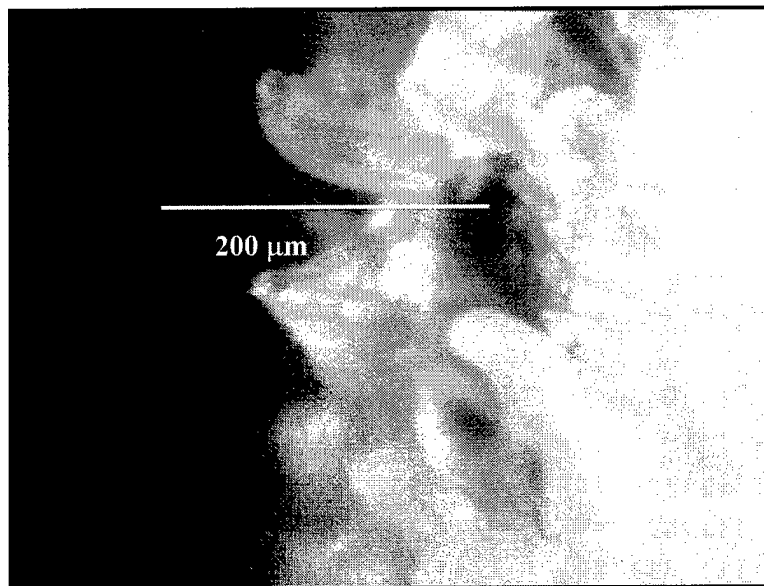


**Figure 16: Ice needle after irradiation. The image size is 470 x 350 μm.**

## 4.0 Oxygen Formation Experiments—Results and Analysis

A theory about the origin of O<sub>2</sub> on Ganymede suggest that ion bombardment of the surface leads to the formation of molecular oxygen trapped within the ice. This theory [Johnson and Jesser, 1997] proposes the gas may be trapped in bubbles and voids, in “microatmospheres”, within the ice layer. The bubbles would tend to aggregate under irradiation by energetic ions aided by thermal annealing, leading to O<sub>2</sub> densities comparable to the solid state. “Solid” oxygen in this form could explain the oxygen absorption bands seen on Ganymede. Using the apparatus and methods described so far, we attempted to verify the ability of 100 keV protons to produce and trap O<sub>2</sub> within thin water ice films.

### 4.1 Reflectance results

Proton bombardment of our water ice films caused morphological changes in the ice, shown most dramatically in the CCD images of the crystalline film, but apparent also in amorphous films. The opacity (where the beam struck the target) was the visual evidence of new scattering centers created by the protons within the films. These scattering centers changed the smooth spectrum of the quartz-halogen lamp to the jagged ratio shown in Figure 17, effectively masking any faint absorption bands from trapped oxygen.

The features depicted in Figure 17 were not reproducible from experiment to experiment. For this reason, we believe the maxima and minima were caused by complex constructive and destructive interference patterns arising from the new scattering centers and surface roughness due to irradiation. We compare the results of this water ice film with the absorption spectrum of a pure, 40 μm-thick oxygen film, shown in Figure 18.

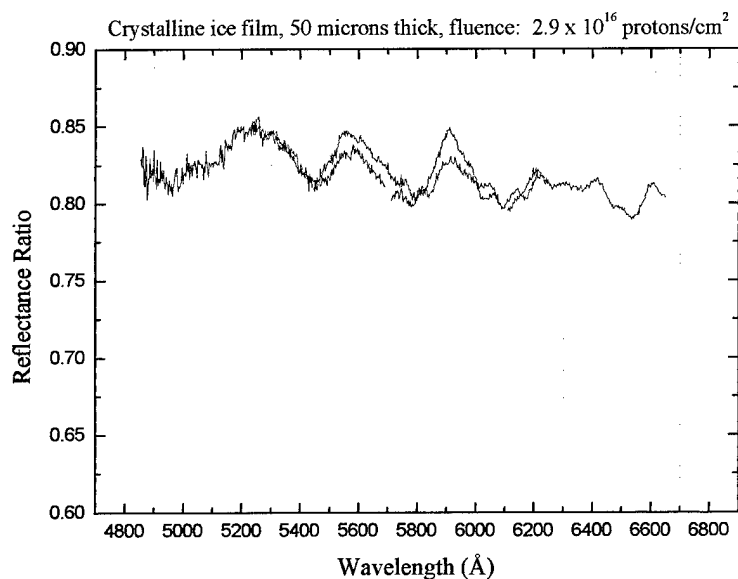


**Figure 17:** Ratio of the reflectance of a bombarded water ice film to that of the film before irradiation. The 50  $\mu\text{m}$  film was grown at 150 K then cooled to 60 K for irradiation.

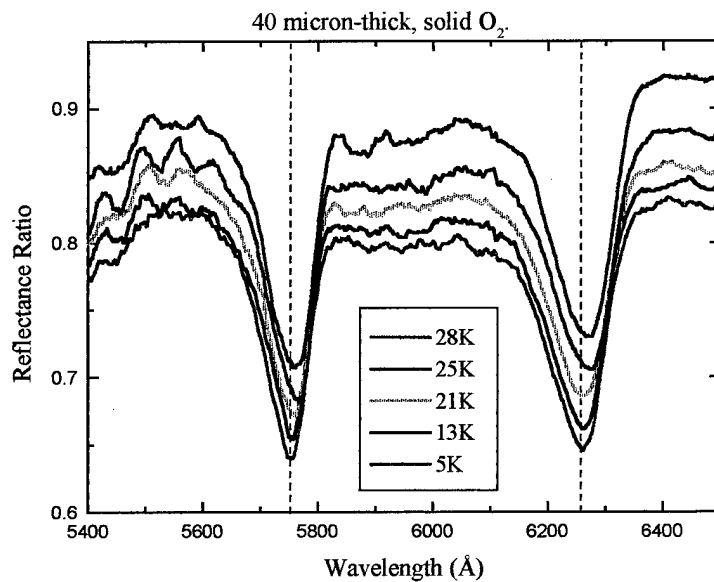


**Figure 18:** Absorption bands for pure O<sub>2</sub> at various temperatures. Note the slight shifts in band position that are due to the formation of different phases of solid oxygen. Spectra have been displaced vertically for clarity.

Note that this film has absorption features an order of magnitude stronger than those detected on Ganymede. If we imagine the two bands being a tenth of the strength shown, they would be lost among the peaks and valleys of the bombarded water ice spectrum in Figure 17.

The results of our reflectance experiments do not rule out the possibility that protons create and trap oxygen in pure water films. However, we realized we would be unable to identify the faint absorption bands expected from ion irradiation. In conclusion, our optical spectrometry investigations detected physical changes in the ice, rather than any chemical changes.

#### 4.2 TPD results

Since we were unable to detect low concentrations of oxygen using reflectance, we switched to TPD experiments on pure water ice films. In preliminary trials, we grew amorphous and crystalline films, bombarded some with protons and left others as controls, then desorbed the films to determine the amount of oxygen generated by protons. Our initial results were suspect, since we found all ices released significant amounts of O<sub>2</sub>, whether they were amorphous or crystalline, irradiated or not. The control films contained an unexpected quantity of O<sub>2</sub> “contaminant”, apparently from background gas in the vacuum chamber. This contaminant interfered with our ability to measure the results of the proton irradiation, since we had could not discriminate between contaminant oxygen and oxygen that may have been produced in the ice by irradiation. As a solution, we switched to an isotope of water, composed of 95% H<sub>2</sub><sup>18</sup>O. During TPD experiments, we could monitor *Mass 36* with the RGA, rather than *Mass 32*, allowing us to eliminate this contaminant.

After changing our water source, we grew two 20 μm-thick amorphous films at 70 K. The first film we desorbed without irradiation, the second we bombarded with  $2.9 \times 10^{16}$  protons/cm<sup>2</sup> at 70 K before desorption. During TPD, we heated the samples at



1.5 K/min and measured the yields of Mass 36  $O_2$  from the two films. Figure 19 depicts the TPD results; the two films showed remarkably similar  $O_2$  desorption yields.

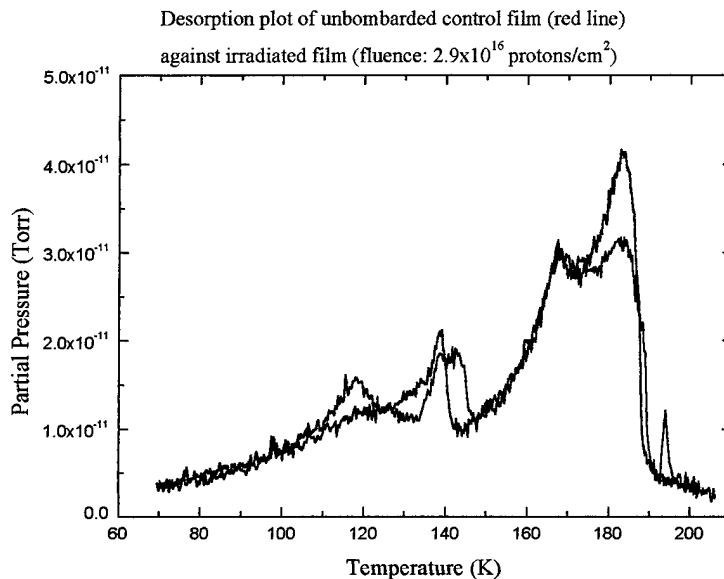


**Figure 19: Mass 36 yields from two 20  $\mu\text{m}$  amorphous ice films at 70 K. The red film was unbombarded, while the black film received a fluence of  $2.9 \times 10^{16}$  protons/cm<sup>2</sup>.**

Clearly, we still had a problem; this time our control film showed unexpected Mass 36. To identify the Mass 36 source, we leaked isotopic water directly into the chamber while carefully monitoring pressures with the RGA. We determined the Mass 36 was  $O_2$  produced by the RGA itself. When electrons in the RGA collide with water molecules, they form a certain amount of atomic oxygen by dissociation, also referred to as “cracking”. Oxygen atoms then combine into molecular oxygen (likely at a surface) and the  $O_2$  is subsequently detected by the RGA at Mass 36. We found that the  $O_2$  signal was 900 times smaller than the water signal.

Using the data from the experiment described in Figure 19 above, we calculated an upper limit on the quantity of molecular oxygen created and trapped in water ice by proton bombardment. We subtracted the  $O_2$  yield of the control film molecules from that of the

irradiated film, and divided the difference by the number of incident protons. We thus determined an *upper limit* of 0.04 molecules O<sub>2</sub> per 100 keV proton at 70 K. The inability to create and trap oxygen within ice agrees with similar irradiation experiments using electrons [T. Orlando, private communication]. It is possible the incident protons created oxygen molecules, but that any such molecules were sputtered immediately.

Sputtered oxygen might be part of the answer to the absorption bands observed on Ganymede, since these low energy molecules would remain bound gravitationally to the satellite and could form a tenuous atmosphere. Such an oxygen atmosphere might condense on the coldest surfaces (the highly reflective patches of water ice), providing sufficient molecular density for the observed bands [Baragiola and Bahr, 1998].

## 5.0 Ozone Experiments – Results and Analysis

The microatmosphere theory mentioned at the beginning of the previous chapter attempts to explain also the ozone-like absorption features discovered on some of the icy moons in the outer solar system [Johnson and Jessor, 1997]. The O<sub>2</sub> bubbles trapped in the ice could serve as a source for O<sub>3</sub> production from both photon and ion irradiation. Alternatively, the theory describing condensed oxygen on very cold (<55 K) icy areas [Baragiola and Bahr, 1998] might explain the origin of the detected ozone bands. In this chapter, we describe laboratory experiments that attempted to duplicate, in the laboratory, the depth, width, and wavelength position of these Hartley bands. We also include desorption data as supporting evidence for the formation of ozone.

### 5.1 Water Ice Films

We began our “search for ozone” by performing reflectance experiments on irradiated, pure water ice films (H<sub>2</sub><sup>18</sup>O). Ozone could be formed from water by the following reactions:

- (1) Radiation + H<sub>2</sub>O → OH + H
- (2) Radiation + OH → O + H

[an unlikely alternative to (1) and (2) is: Radiation + H<sub>2</sub>O → H<sub>2</sub> + O]

- (3) O + O + H<sub>2</sub>O → O<sub>2</sub> + H<sub>2</sub>O
- (4) O + 2O<sub>2</sub> → O<sub>3</sub> + O<sub>2</sub>

However, O<sub>2</sub> formation competes with the following reactions:

- (5) O + 2 H<sub>2</sub>O → H<sub>2</sub>O<sub>2</sub> + H<sub>2</sub>O
- (6) O + OH + H<sub>2</sub>O → HO<sub>2</sub> + H<sub>2</sub>O
- (7) O + H + H<sub>2</sub>O → OH + H<sub>2</sub>O

The competition among these equations must be responsible for the very low  $O_2$  production yield noted in the previous chapter.

As can be seen from the equations, the production of molecular oxygen is a precursor for the formation of  $O_3$ . We already showed that proton bombardment of water ice films was *not* sufficient to produce measurable  $O_2$  absorption bands in the visible. However, molecular oxygen is a weak absorber, so the absence of a band in the visible does not imply the absence of  $O_2$ . We therefore irradiated pure water ice and measured the reflectance ratio to detect any  $O_3$  derived from very small concentrations of  $O_2$ .

As we show in Figure 20 below, our reflectance experiments in the UV on water ice films did not detect an ozone feature. Gerkaines et al. (1996) found similar negative results in UV photolysis experiments on pure water ice. The ozone band (see Section 5.2) should be a broad (~600 Å FWHM) feature centered in the vicinity of 2500-2600 Å. Instead, we found a decreasing trend toward shorter wavelengths, known as a red slope. The slope may be due to absorptions from other species produced in the water ice by irradiation; possible candidates are OH,  $HO_2$ , and  $H_2O_2$ . These species might also account for the possible absorption feature short of 2400 Å.

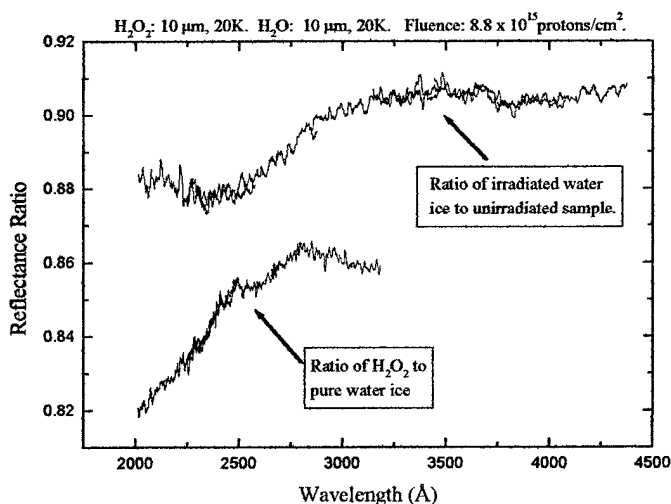


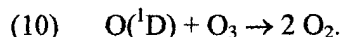
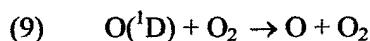
**Figure 20:** Top curve shows the reflectance spectrum of pure water ice in the UV, after irradiation by  $8.8 \times 10^{15}$  protons/cm<sup>2</sup>. Bottom curve: absorption characteristics of unbombarded  $H_2O_2$  in solution.

## 5.2 Oxygen/Water Mixed-Ice Films

Following the water ice experiments, we switched to the oxygen/water mixtures discussed in Chapter 2. The mixed-ice films contained an abundance of O<sub>2</sub>, adding extra possibilities to the chemical reactions discussed in Section 5.1. If we assume our films maintained O<sub>2</sub> densities comparable to the solid state, then we must consider O(<sup>1</sup>D) “quenching” of any O<sub>3</sub> produced [Johnson and Jesser, 1997]. The O(<sup>1</sup>D) atom is an excited product of ozone photolysis:



Instead of following eqn (4) above, the O(<sup>1</sup>D) atom interacts with O<sub>2</sub> and O<sub>3</sub> as follows:



Equations (9) and (10) acts to suppress O<sub>3</sub> formation, limiting the equilibrium concentration of O<sub>3</sub> possible in the film. Johnson and Jesser (1997) found the concentration equilibrium to be  $[\text{O}_3]/[\text{O}_2] \approx 2 \times 10^{-4}$  for oxygen/water mixtures at 120 K, a number which has been recently corrected to  $10^{-2}$  [R. Johnson, personal communication].

The ultraviolet reflectance spectra lacked the noise that characterized our experiments with water ice. We believe the scattering centers created by proton impact (the broken safety glass effect) do not produce significant constructive and destructive interference in these mixed-ice films. The smoother data worked to our advantage, enabling us to discern the Hartley band at levels as low as 2% absorption. Such sensitivity was enough for this investigation, since the Hartley Band detected on Ganymede appears to be about 30% in strength [Noll et al., 1996]. Figure 21 gives an example of a typical data set, showing the overlapping spectra covering the width of the Hartley band generated by proton bombardment.

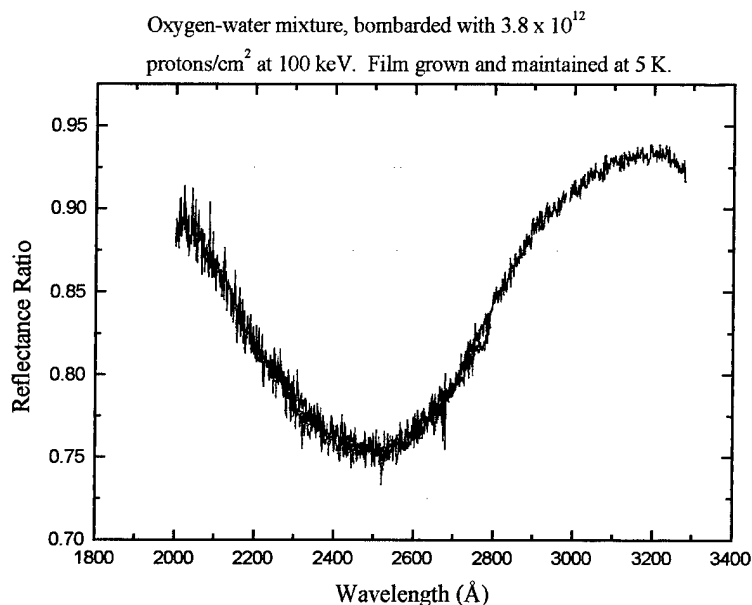


**Figure 21: Typical Hartley band of a 10  $\mu\text{m}$ -thick film showing band depth of 17%.**

We found at low fluences ( $<10^{14}$  protons/cm<sup>2</sup>), the individual spectra lined up well, perhaps needing only slight vertical adjustments ( $<1\%$ ). However, as fluence increased, the overlap became less satisfactory, requiring greater vertical shifts to allow analysis of band depth and minimum position. We account for these shifts using error bars in our summary data that follows. Although we do not fully understand the reason for these mismatches, we believe they are related to fluctuations in lamp intensity and shifts in the background spectra.

Our worst example of spectra mismatching actually occurred with the CO<sub>2</sub> reflectance experiment we conducted after finishing our work on oxygen/water films. The CO<sub>2</sub> experiment was run to gather data on the shape and fluence dependence of the Hartley band in a CO<sub>2</sub> matrix. We use this data later in the thesis for comparison with other films and spectra acquired from Ganymede, Rhea, and Dione. The following two graphs are of the same CO<sub>2</sub> film, the first at a low fluence (Figure 22), and the second at the maximum fluence (Figure 23).

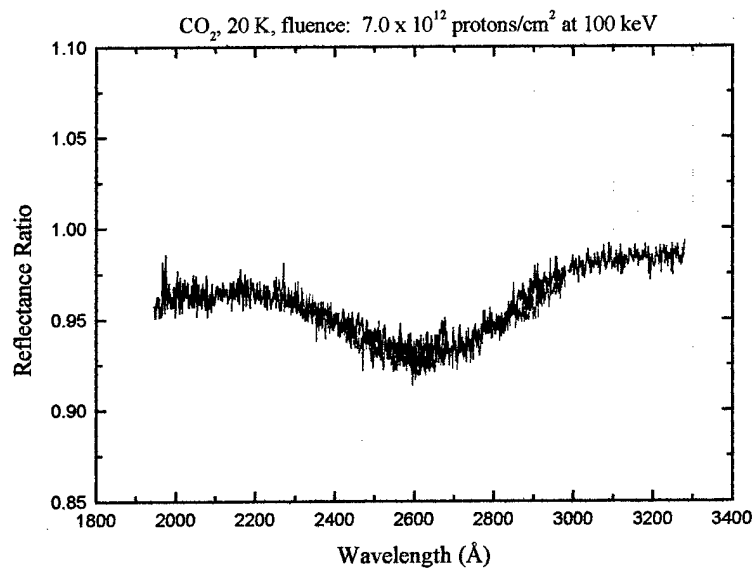


**Figure 22: Low fluence irradiation of a 50 μm-thick CO<sub>2</sub> film.**

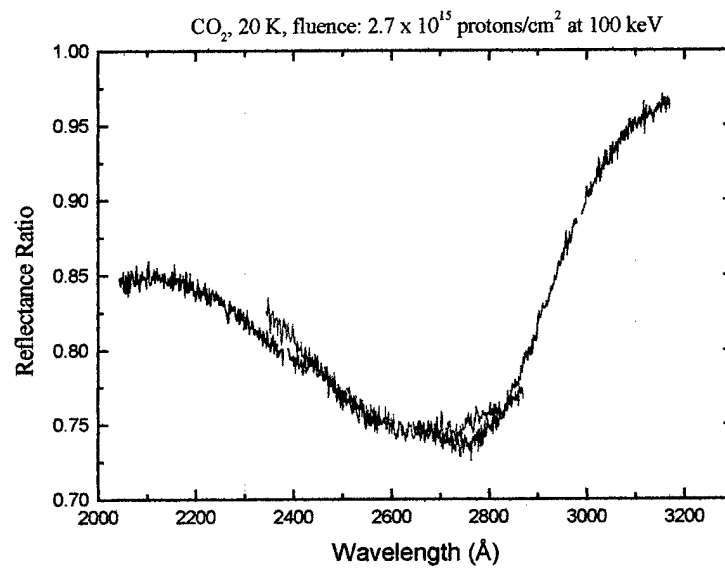


**Figure 23: High fluence irradiation of a 50 μm-thick CO<sub>2</sub> film.**

In Figure 23, we have shifted the individual curves to match as well as possible. Notice that the vertical mismatch after shifting is only about 2%. The result is a slight smearing of the minimum position, without any significant impact on the band depth.

Our goal in investigating oxygen/water films was to characterize the shape, depth, and wavelength position of the Hartley band as a function of film temperature and proton fluence. Consequently, we ran six trials covering a temperature range from 5 K to 50 K, where each film was subjected to incrementally increasing fluences (see Figure 24). At all temperatures, we saw a rapid increase in band depth at proton fluences well below the maximum estimated value on Ganymede ( $\sim 10^{16}$  protons/cm<sup>2</sup>), a value that results from the equilibrium of ion irradiation and erosion by micrometeorites. Although the absorption bands increased initially, they approached a plateau in each experiment. The plateau value was dependent upon temperature; colder films demonstrated significantly greater absorption than warmer films.

Band saturation masked the true absorbance at high fluences, so raw data needed to be corrected to obtain absorbance values. According to Beer's Law, photon absorption obeys the equation:  $I = I_0 e^{-\alpha L}$  where  $I_0$  is the incident light intensity,  $I$  is the intensity after passing a path length  $L$  and  $\alpha$  is the absorption coefficient. The normalized absorption is then:

$$A = e^{-\alpha L}$$

We obtain the effective absorbance  $\alpha L = -\ln A$  and plot the values in Figure 25. The line shapes are similar to those in Figure 24, but notice at high fluences the lines representing the different temperatures become more separated.



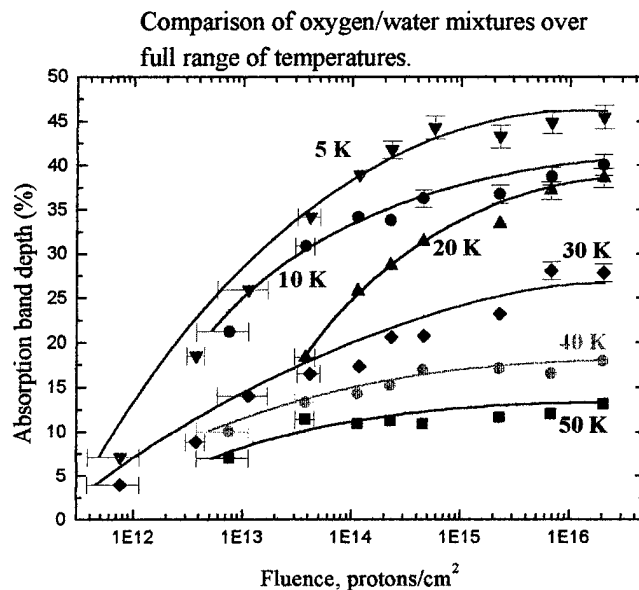


**Figure 24:** Summary plot of all six trials. Vertical error bars at the highest fluences account for uncertainty due to shifts in the spectra. All other points have a vertical error of 2%.

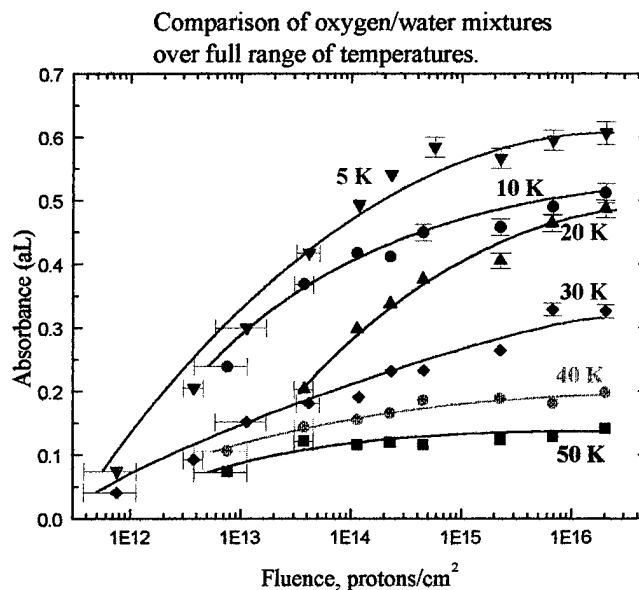


**Figure 25:** Results corrected for saturation by plotting absorbance rather than Hartley band depth.

As shown in the previous two charts, band depth (and absorbance) both depended upon the temperature of the film *during* irradiation. In Figure 26, we show instead the temperature dependence of the band *after* irradiation, as an oxygen/water mixture film was warmed.

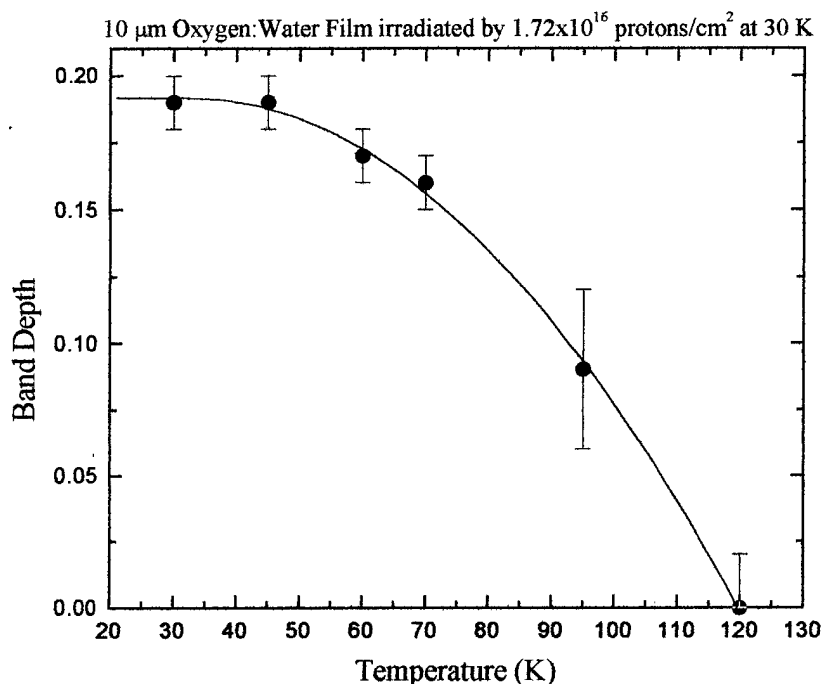


**Figure 26:** Evolution of the Hartley band in an irradiated film as it was warmed. Warming rate was approximately 1.5 K/min. Temperature ramp was paused at the indicated temperatures to take reflectance spectra.

We return to a question posed earlier in the paper on the possible effects of proton current: were our high laboratory currents creating additional effects? To test for current effects, we added two extra data points at the beginning of the 5 K and 30 K experiments. For these points, we reduced the current by an order of magnitude to 50 nA. Referring to Figure 24, the extra points show up on the left side of the chart for the 5 K and 30 K lines. Since the extra points appear to fit well with the rest of their respective curves, we concluded that the value of the

current in this range has no noticeable effect on absorbance. Of course, the current is still higher than that at Ganymede, but we believe we could continue to reduce our currents without changing the results mentioned so far.

The next series of graphs (Figure 27) demonstrates the fluence dependence of the Hartley band for an  $\text{H}_2\text{O}:\text{O}_2$  film at 30 K. The 30 K results were typical of the experiments in general.

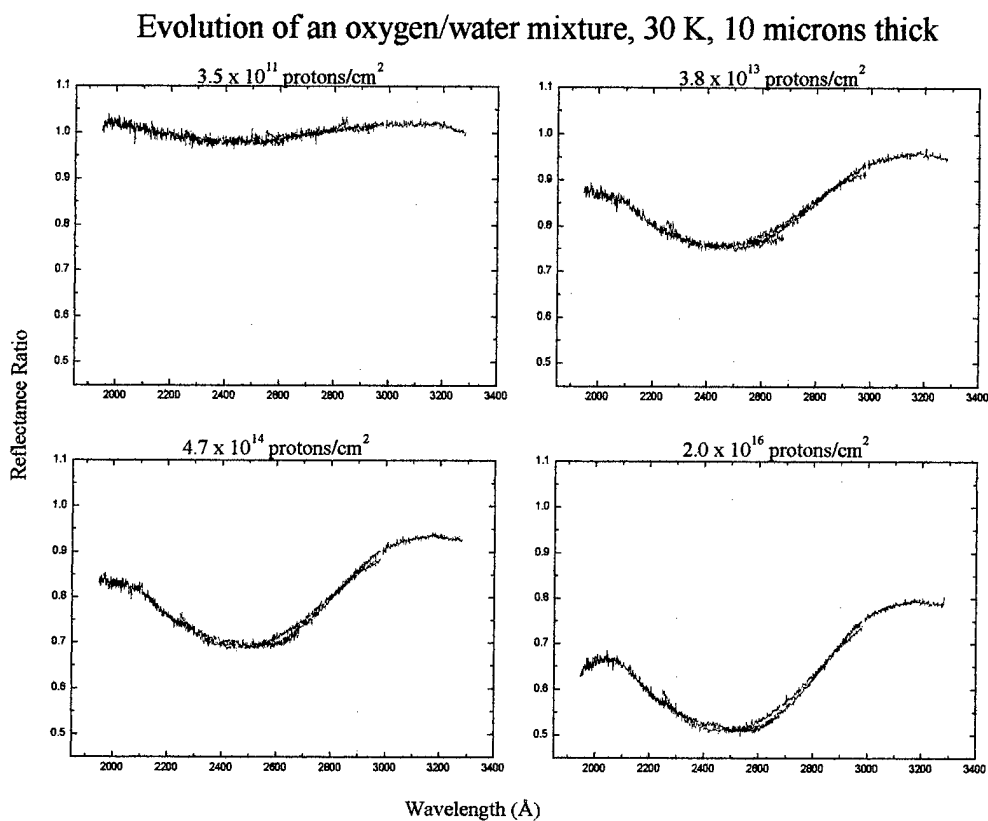


**Figure 27: Changes in the reflectance of a 10  $\mu\text{m}$  oxygen/water mixed-ice film, grown and irradiated at 30 K.**

The figure highlights several of the main findings in our study. First, band depth clearly evolved with increasing fluence, as we have already. Second, the overall reflectance of the film at the band ends declined. This "darkening" may be the same phenomenon we saw in the UV

reflectance of irradiated water ice, giving the “red slope” in Figure 20. Third, the position of the band minimum value ( $\lambda$ ) appeared to shift with increasing fluence.

To further characterize this third point, we had to consider the “background slope” of the spectral data which distorts the position of the *actual* band minimum (see Figure 28). This correction (the largest shift was 50 Å for the 30 K film) required some data manipulations that we now discuss.

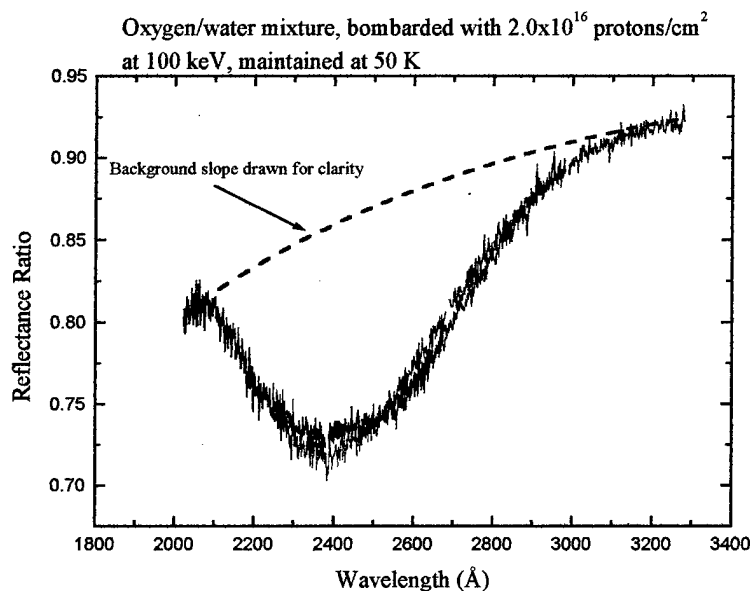


**Figure 28: Depiction of background slope.**

In spectral analysis, a background slope such as the one in Figure 28 makes the minimum position look further to the left than it actually is. To correct for this distortion, we selected several data points at each end of the line shape and fit a second-order polynomial curve to these points. It was then possible to subtract the spectra from this polynomial “slope”, giving a modified Hartley band that was “level” at each end. Band depth did not change appreciably with this slope correction since the band was so broad. However, the minima position did shift to a longer wavelength each time (for the 50 K curve shown above, the shift was almost 45 Å). In Figure 29 below, we show the slope fit and subtraction procedure.

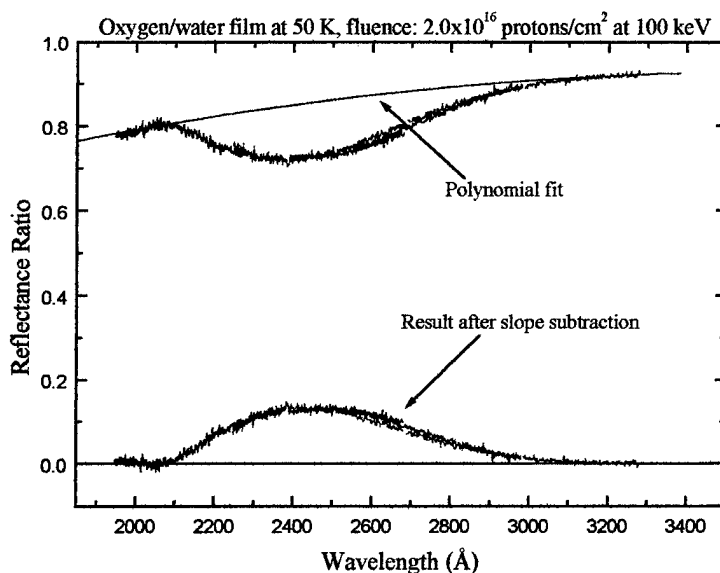


**Figure 29: Slope subtraction procedure, giving a band that is “level” at both ends.**

After correcting the band shapes for background slope, we plotted the minima positions as a function of fluence, *and* the temperature of the oxygen/water films. Figure 30 presents the results of this analysis. Values for the minima ranged from 2425 Å to 2585 Å, and showed both a temperature and fluence dependence. In all trials except at 50 K, the minima shifted to longer wavelengths with increasing fluence (the 50 K film showed no shift). The greatest shift in any one experiment was approximately 110 Å, for the 20 K film.

We also found the minima shifted to longer wavelengths as film temperature *decreased*. This correlation between temperature and band position raised the possibility of estimating the temperature of ozone on a distant body. To investigate this avenue, we subtracted the background slope from the Rhea absorption band [Noll et al., 1997] (see Figure 3), and determined the minimum to be ~2625 Å. The same value holds for Dione. The band minimum on Ganymede is ~2575 Å in the HST observations [Noll et al., 1996], but ~2700 Å in the Galileo measurements [Hendrix et al., to be published]. When we compared these minima positions with those of our laboratory experiments, we found the 5 K film to be the closest match. Since such a low

temperature does not seem feasible even in the polar regions of these moons, we realized some other mechanism or environment must be at work. Further studies were clearly advised.

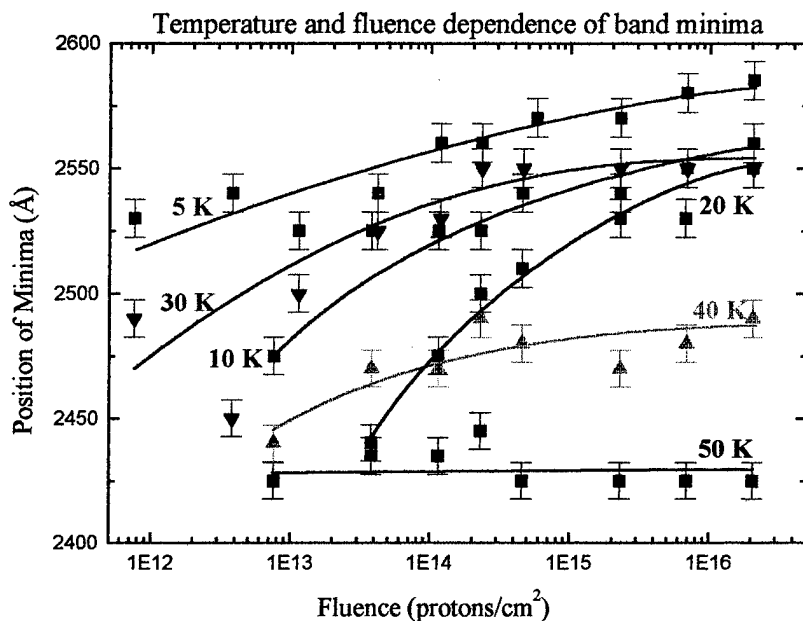


**Figure 30: Position of the Hartley band minima as a function of fluence and temperature. Vertical error bars depict uncertainty due to the breadth ( $\sim 600$  Å FWHM) of the Hartley band.**

### 5.3 Other Ices

Therefore, we ran parallel experiments on three other types of films, looking for comparisons with the mixed ice films we had already investigated. Thus, we grew one film of pure carbon dioxide ( $50 \mu\text{m}$  thick), one of pure oxygen ( $25 \mu\text{m}$  thick), and one from a 30% solution of hydrogen peroxide in water ( $10 \mu\text{m}$  thick). The carbon dioxide and hydrogen peroxide films were both grown and irradiated at 20 K, the oxygen film at 5 K to minimize sublimation. Irradiation for the  $\text{CO}_2$  and  $\text{O}_2$  films was accomplished at 50 nA, giving us more accurate control over total fluence. Since we had not worked with these species before, we wanted to avoid

destroying the films before we could gather reflectance data. The  $\text{H}_2\text{O}_2$  film underwent 500 nA bombardment, as we expected it to behave like normal water ice under irradiation. The  $\text{CO}_2$  and  $\text{O}_2$  films were similar in appearance: both bright white and smooth in texture. The  $\text{H}_2\text{O}_2$  film looked rougher, but was also bright, much like amorphous water ice films.

We note in Figure 31 below that absorption due to ozone in the  $\text{H}_2\text{O}_2$  and  $\text{O}_2$  films approached a plateau (comparable to the oxygen/water films), while the feature in the  $\text{CO}_2$  film was not level by the end of the experiment. The oxygen film exhibited the strongest absorption at the fluences we measured, although  $\text{CO}_2$  might have overtaken  $\text{O}_2$  at higher fluences. A comparison between Figures 31 and 24 shows an interesting aspect: the pure oxygen film did not exhibit an absorption band as deep as the parallel oxygen/water mixture (5 K).

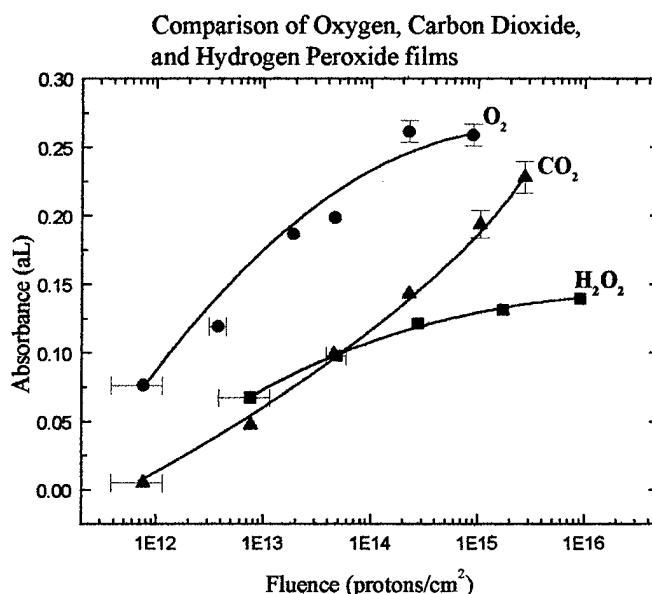


**Figure 31: A comparison of absorbance due to ozone in the three “other ices”.**

Next, we compare in Figure 32 the line shapes of these three films with the Hartley bands of the oxygen/water mixed-ice films. Notice that the minima for  $\text{CO}_2$  and  $\text{O}_2$  are similar, and both fall to longer wavelengths than the bands of the oxygen/water films we examined. The minimum for the 20 K  $\text{H}_2\text{O}_2$  film matches quite well with that of the 20 K oxygen/water film ( $\sim 2550 \text{ \AA}$ ).

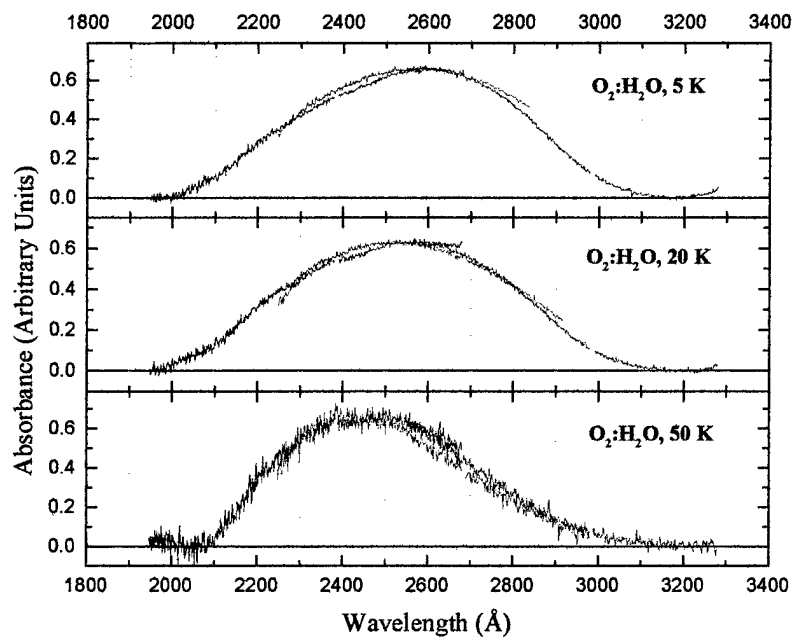
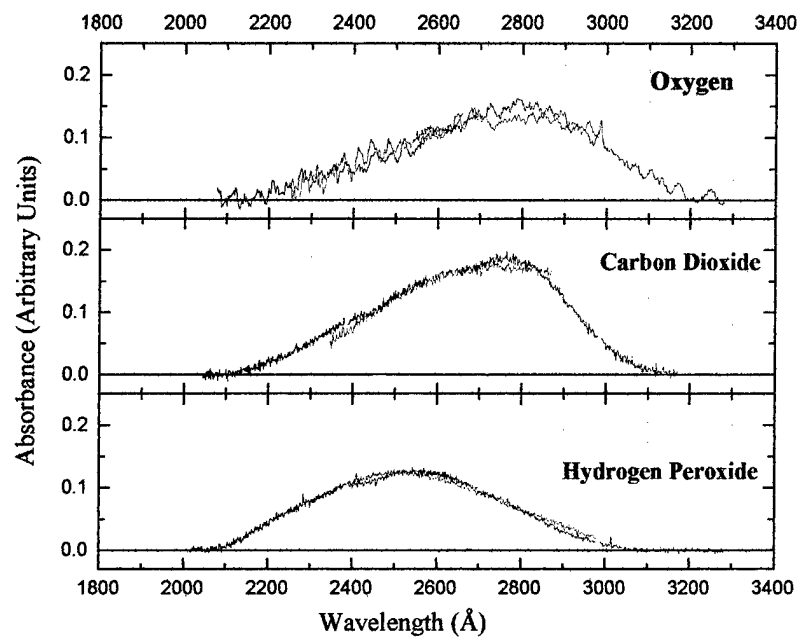


**Figure 32: Illustration of Hartley band minima for various films. Y-axis units are arbitrary in these plots.**



We characterized the  $\text{H}_2\text{O}_2$  film further by determining what proportion of the film was actually hydrogen peroxide (mass 34). At 70 K, the temperature of our continuously baked manifold assembly, a 30%  $\text{H}_2\text{O}_2$  solution in water yields a vapor pressure that is only 2%  $\text{H}_2\text{O}_2$  [Schumb et al., 1955]. During film growth, we used the RGA to monitor the pressures of both  $\text{H}_2\text{O}$  and  $\text{H}_2\text{O}_2$ , and found a 0.5%  $\text{H}_2\text{O}_2$  concentration relative to the water, in fairly close agreement with the reference cited above. We determined from our previous reflectance experiments on "pure" water ice films that protons are not efficient at producing and trapping ozone in a water matrix (we detected no measurable absorption band). However, by adding only a 0.5% concentration of  $\text{H}_2\text{O}_2$ , protons produced enough ozone to generate a 14% Hartley band.

Concluding the section on ozone reflectance experiments, we present Figures 33, 34 and 35 which give absorption band shapes of our laboratory films layered with new data from the Galileo Ultraviolet Spectrometer, previous data from HST, and curves on gaseous and solid ozone. The new Ganymede data, reported by A. Hendrix et al. [to be published], shows the Ganymede absorption band considerably red-shifted in comparison with previous HST data on Ganymede. The difference between the Galileo and HST spectra has not yet been explained. We note that no single band shape from our laboratory experiments provides a good match with the astronomical data from Ganymede.

In Figure 33, the width and wavelength position of the feature from Ganymede suggest that the Hartley band may actually be composed of the absorptions due to *several* different species, possibly including sulfur compounds [Hendrix et al., to be published]. In Figure 34, we show a close agreement between our 50 K mixed-ice film and the published absorption data for solid  $\text{O}_3$ . We believe the 50 K film, the warmest of all our trials, lost much of its oxygen over the course of the experiment, leaving only pure  $\text{O}_3$  and water ice. Finally, Figure 35 compares the 50 K mixed-ice film with the HST data, showing how multiple absorbers might explain the width of the Hartley band on Ganymede.

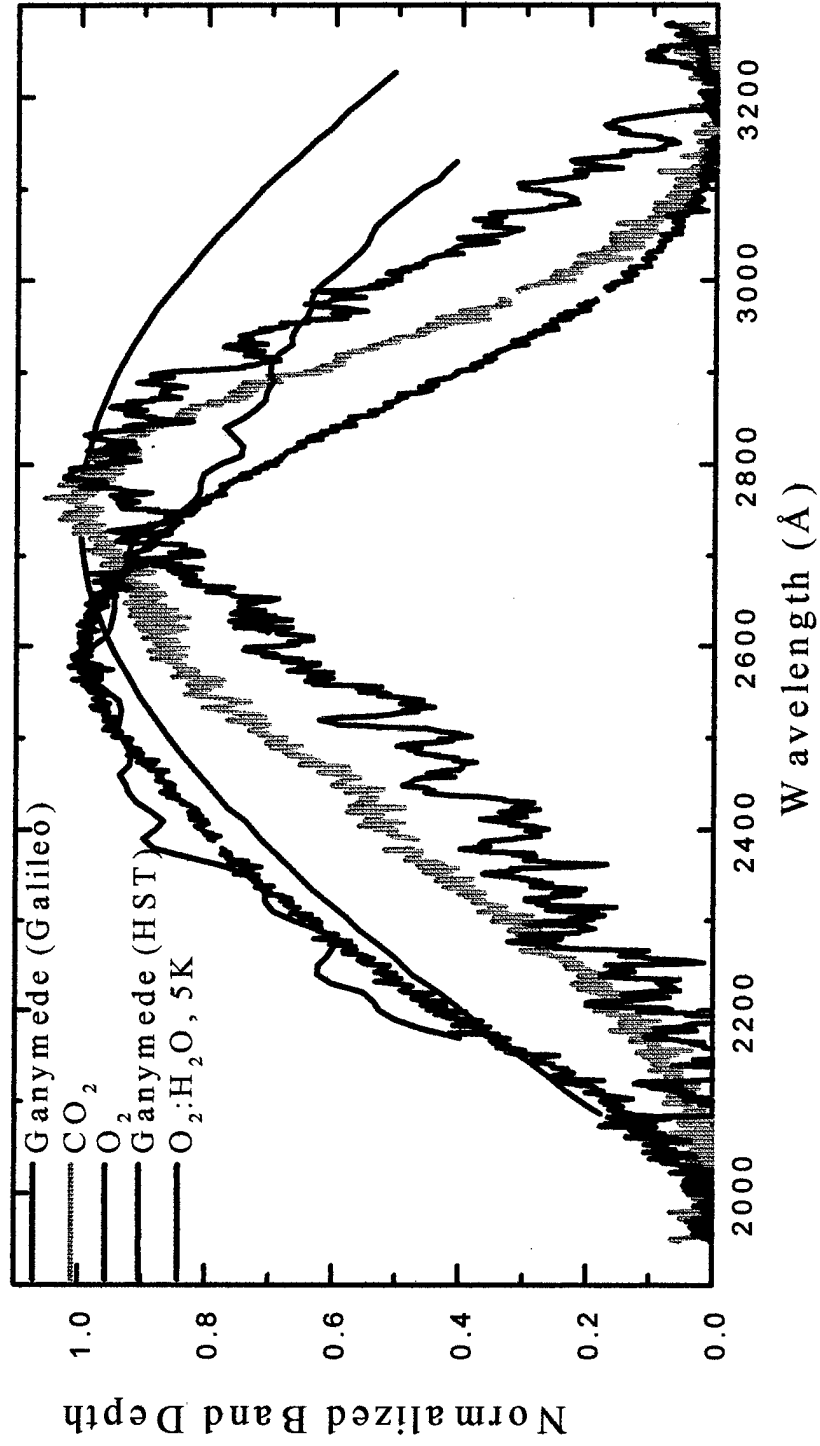


Figure 33: Blue line shows new data from Galileo [Hendrix et al]. Notice that the absorption is red-shifted in comparison with previous HST data.

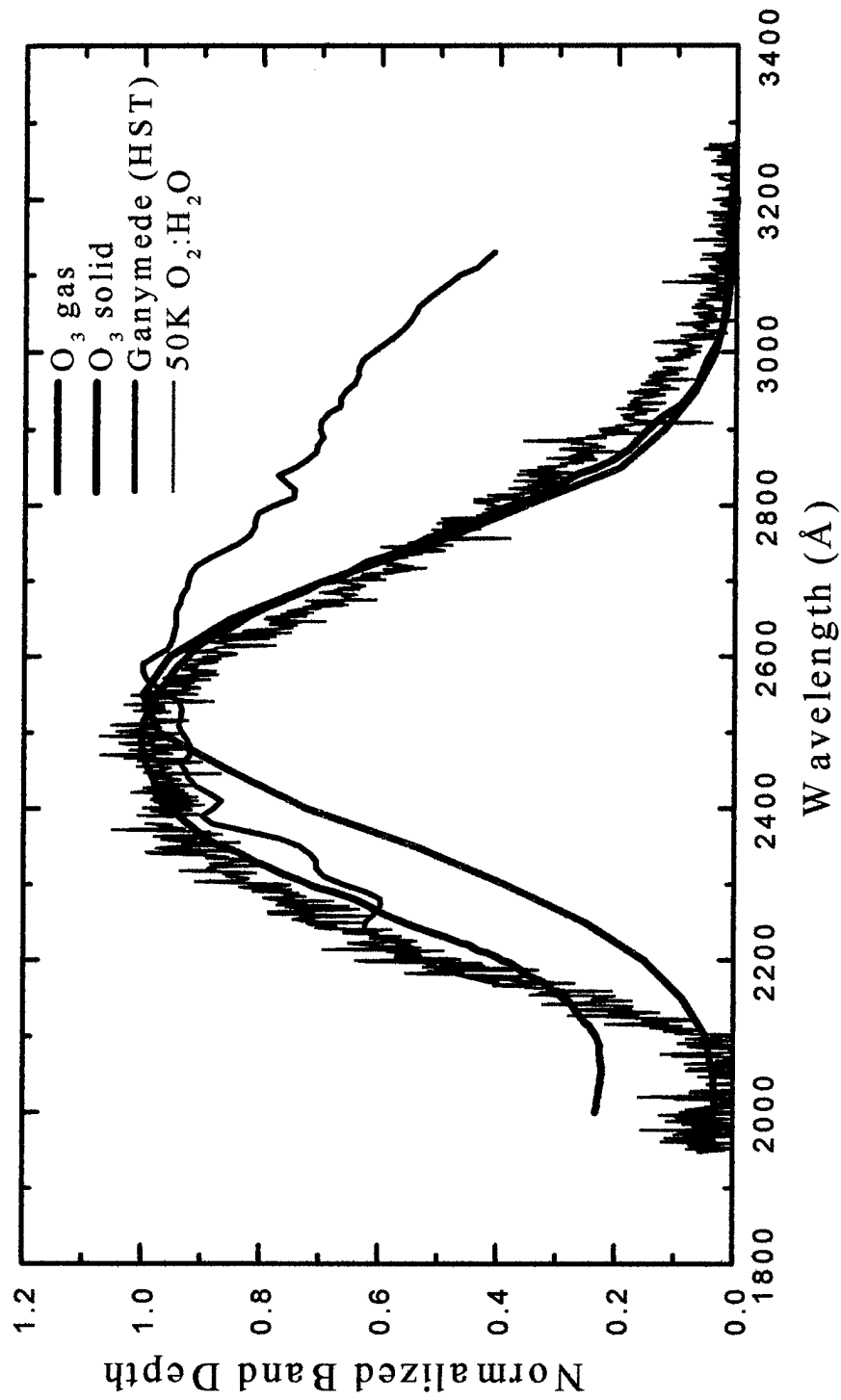
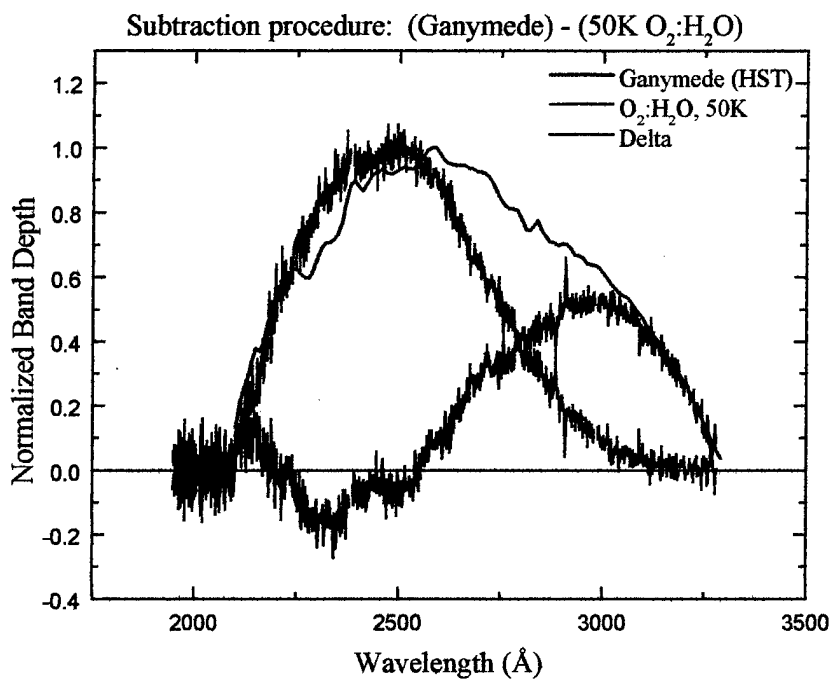


Figure 34: Agreement between 50 K O<sub>2</sub>:H<sub>2</sub>O film and solid O<sub>3</sub>, O<sub>3</sub> solid (10 K) from Sedlacek and Wight (1989); O<sub>3</sub> gas from Okabe (1978); HST from Noll et al. (1996).



**Figure 35:** Black line indicates the difference between the band on Ganymede [Noll et al., 1996] and the 50 K mixed-ice film. The plot suggests the presence of other absorber(s) in the vicinity of 3000 Å.

### 5.4 TPD Results for Ozone Experiments

To finish characterizing the films, we present the TPD data from the various experiments. TPD data for all oxygen/water films showed a steep, but brief, initial outgassing of ozone, followed by a more gradual desorption above 100 K. The final peak, around 195 K, coincided with the complete desorption of the entire film. Figure 34 depicts the data for the 30 K film.

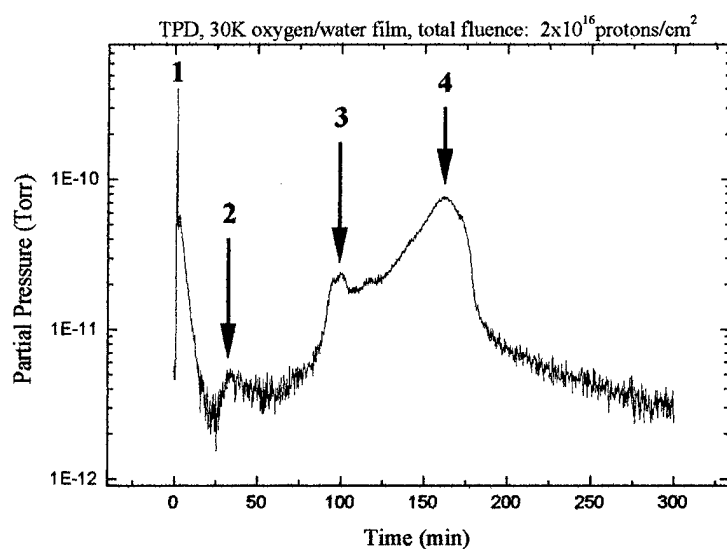


**Figure 36: Thermal desorption data showing  $O_3$  evolved from a 10  $\mu\text{m}$  thick oxygen/water mixture film. Heating rate was approximately 1.1 K/min. Peak 1 was due to a large, initial outgassing of  $O_2$ ; Peak 2 ( $\sim 69$  K) was ozone sublimating from the *surface*; Peak 3 ( $\sim 135$  K) coincides with the transformation from amorphous to crystalline ice; Peak 4 ( $\sim 195$  K) corresponds to the complete desorption of the ice film.**

We also include desorption plots for the  $H_2O_2$  and  $CO_2$  films for comparison. The hydrogen peroxide film (Figure 35) exhibited an ozone trace very similar to that of the oxygen/water film in Figure 34. Along with the ozone trace, we plot oxygen and hydrogen

peroxide, both of which desorbed from this film as well. In the graph of the  $\text{CO}_2$  film (Figure 35), we include desorbed oxygen with the ozone trace.

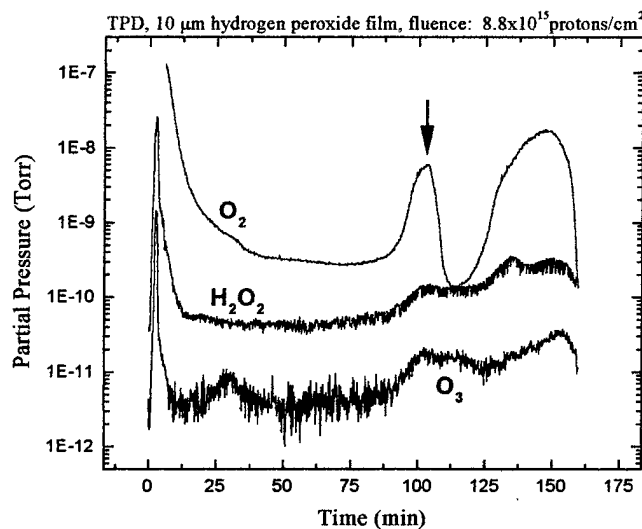


**Figure 37:** Plot of the desorption data from an irradiated  $\text{H}_2\text{O}_2$  film, starting at 20 K. Warming rate was  $\sim 1.1$  K/min. The peak indicated by the arrow was at 136 K; at  $t = 155$  minutes, film temperature was 195 K.

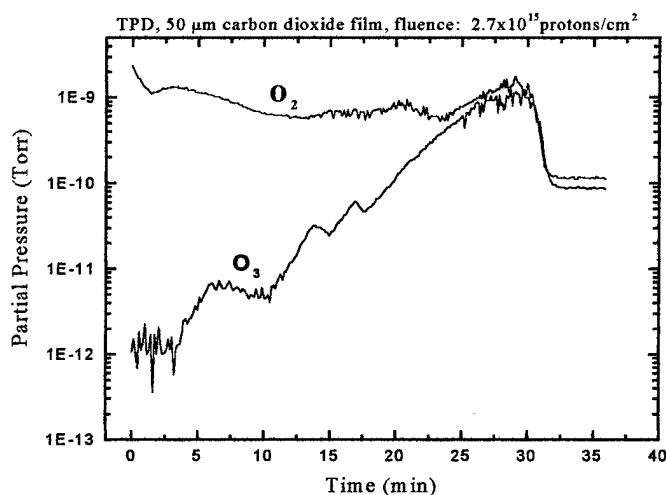


**Figure 38:** Plot of the desorption data from an irradiated,  $\text{CO}_2$  film, starting at 20 K. Warming rate was  $\sim 2$  K/min. At  $t = 28$  minutes, the temperature was 73 K.

Finally, we compare our TPD results with results from the reflectance experiments (see Table 1 below). TPD values were calculated as described in Section 2.5, and include an error of 50%. Reflectance results are described in terms of the optical column density of ozone in each film. Optical column density is related to absorbance as follows:

$$\alpha \cdot L = \sigma \cdot N \cdot L$$

where  $\alpha L$  is the absorbance calculated earlier,  $\sigma$  is the photoabsorption cross-section,  $N$  is the molecular density, and  $L$  is the optical path length. The product  $NL$  is the optical column density, and using a value of  $\sigma = 1.0 \times 10^{-17} \text{ cm}^2/\text{molec}$  for  $\text{O}_3$  [Okabe, 1978], we can calculate the value of  $NL$  for each of our films.

Film Composition	Fluence ( $10^{16} / \text{cm}^2$ )	TPD ( $10^{16} \text{ O}_3/\text{cm}^2$ )	NL ( $10^{16}/\text{cm}^2$ )
Mixed, 5 K	2.1	1.8	6.1
Mixed, 10 K	2.1	2.2	5.1
Mixed, 20 K	2.1	2.1	4.9
Mixed, 30 K	2.1	2.3	3.3
Mixed, 40 K	2.1	1.5	2.0
Mixed, 50 K	2.1	0.48	1.4
$\text{H}_2\text{O}_2$	0.88	1.7	1.4
$\text{CO}_2$	0.28	7.7	2.3
$\text{O}_2$	0.091	1.3	2.6

**Table 1: Comparison of TPD results with reflectance results.**

Notice how similar the TPD results are for the six mixed oxygen/water films. Only in the warmest film (50 K) was there an apparent decrease in ozone concentration, probably attributable to the high oxygen outgassing at this temperature that we also observed during film growth.

If the ozone content of all these mixed-ice films was approximately the same, how do we explain the temperature dependence of Hartley band depth (as evidenced by the "NL" values in Table 1)? We had thought initially that the warmer films, retaining lower oxygen concentrations

throughout the experiment, yielded a lower production of ozone under proton irradiation. The data in Table 1 refutes that hypothesis.

What else might be causing the greater band-depths at lower temperatures? The literature does not indicate any temperature dependence in the ozone photoabsorption cross section, so we discount that possibility. An explanation might be a temperature dependence in the *structure* of the film, giving longer optical path lengths for the coldest films, permitting greater absorption.



## 6.0 Conclusions

Proton irradiation of thin ice films caused morphological and chemical changes, which we determined using optical microscopy, reflectance spectroscopy and thermal desorption experiments. With a long-distance microscope, we examined the growth and microstructure of amorphous ice films, noting the presence of grains and “needles”. We also imaged the morphological changes the proton beam created in a crystalline ice film, turning the transparent film opaque. This observation agreed with our reflectance results in the visible range: bombardment of pure water ice films increased the number of scattering centers. These features made our reflectance ratios “noisy” (~5%), hindering the detection of faint O<sub>2</sub> absorption bands.

In addition to the reflectance experiments, we characterized the water ice films with the RGA. We grew ice films and bombarded them with 100 keV protons to fluences on the order of equilibrium fluences expected on the surface of Ganymede (~10<sup>16</sup>/cm<sup>2</sup>). After the irradiation period, we thermally desorbed the films and found that they appeared to contain equivalent concentrations of oxygen, regardless of film temperature, ice structure (amorphous or crystalline), and fluence. In fact, control films that we desorbed without *any* irradiation contained this oxygen as well. We concluded that the O<sub>2</sub> was not in the film, but was produced by electron bombardment in the RGA, followed by recombination. We obtained an *upper limit* on the number of O<sub>2</sub> molecules (produced by 100 keV protons) that stayed within the film: 0.04 O<sub>2</sub>/proton at 70 K. This low value may be due to fast reactions of radiolytic atomic oxygen with other radicals and water molecules in the ice films.

Since our water ice films seemed to have low levels of included molecular oxygen, we attempted to create ozone directly from the films by proton irradiation. Our reflectance results showed no feature that might be described as an ozone-like absorber. We did notice an overall decrease in reflectance in the ultraviolet, as well as a red-slope shortward of ~3500 Å. The

darkening and the slope may have been due to other species created within the ice by the protons: OH, HO<sub>2</sub>, and H<sub>2</sub>O<sub>2</sub>. We concluded that 100 keV protons do not generate significant ozone directly from pure water ice.

We irradiated oxygen/water mixed ice films at a range of temperatures (5 K to 50 K). After only moderate fluences ( $\sim 10^{13}$  protons/cm<sup>2</sup>), we detected the Hartley absorption band at all film temperatures. We found the band deepened as a function of fluence, and approached a plateau for each film. The strength of the absorption at the plateau was inversely related to film temperature; our 5 K mixture film showed an absorption band about 3 times deeper than the film at 50 K. Thermal desorption experiments gave the unexpected result that all of the films held comparable amounts of ozone, estimated to be on the order of  $2 \times 10^{16}$ /cm<sup>2</sup>, while reflectance spectroscopy gave a range of values. We concluded that the temperature dependence of band depth does not come from the quantity of ozone generated but from a variation in optical path length among the films at different temperatures.

We noticed that the *position* of the band minimum also depended on fluence and temperature. As fluence increased, the minimum position for each band tended towards longer wavelengths (except for the 50K film, which remained constant). At a given fluence, colder films exhibited minima at longer wavelengths than warmer films. We estimated the Hartley bands at Rhea and Dione to be  $\sim 2625$  Å after background subtraction, and the band at Ganymede to be  $\sim 2575$  Å (these estimates all based on Hubble FOS spectra). According to our experimental data on oxygen/water mixed-ice films, the satellites would have to maintain temperatures near 5 K if the position ( $\lambda$ ) of their respective bands were due only to oxygen trapped within a water matrix. Since 5 K is extremely unlikely, even in polar regions, we looked for a combination of different ices that could generate the wide Hartley band seen on these satellites.

Consequently, we studied the effect of irradiation on reflectance and TPD of three other ices at low temperatures: CO<sub>2</sub>, O<sub>2</sub>, and H<sub>2</sub>O<sub>2</sub>. The band minima positions for CO<sub>2</sub> and O<sub>2</sub> were

red-shifted 200 Å with respect to our coldest oxygen/water film. On the other hand, the H<sub>2</sub>O<sub>2</sub> minimum matched remarkably well with the oxygen/water film of the same temperature.

In conclusion, we demonstrated that ion irradiation of ices of O<sub>2</sub>:H<sub>2</sub>O, O<sub>2</sub>, CO<sub>2</sub>, and H<sub>2</sub>O<sub>2</sub>, but not pure H<sub>2</sub>O, led to the synthesis of ozone. This process may be responsible for ozone formation on icy satellites subject to energetic ion bombardment.

## APPENDIX A – Luminescence experiments

Our apparatus was suited for studying another water ice phenomenon of current interest: irradiation-induced luminescence [Johnson and Quickenden, 1997]. Researchers using 20 eV electrons induced ultraviolet luminescence in water ice under UHV conditions; emission features were *broad* in wavelength, with the strongest emission centered near 400 nm, and a weaker feature short of 300 nm as shown in Figure 37 [Merkel and Hamill, 1971]. We attempted to duplicate these luminescence results using our high-energy protons.

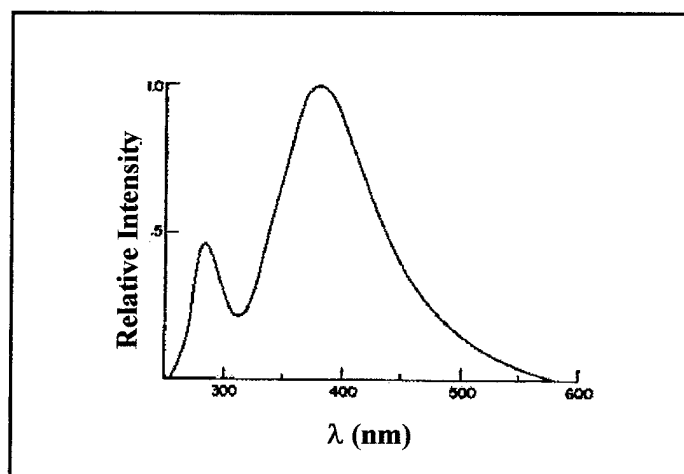


**Figure 39: 20-eV electron-induced luminescence in a 200 Å film of H<sub>2</sub>O at 77° K [Merkel and Hamill, 1971].**

We varied numerous parameters in the luminescence experiments. We grew films at temperatures from 5 K to 150 K, covering the full range of stable ice films in UHV conditions. The films were bombarded, always with 100 keV protons, at angles from normal to 70 degrees oblique. CCD exposure times were ten minutes per image. Other than the sharp feature in Figure 38 below, we were unable to detect any sort of broad-band luminescence from proton interaction with water ice.

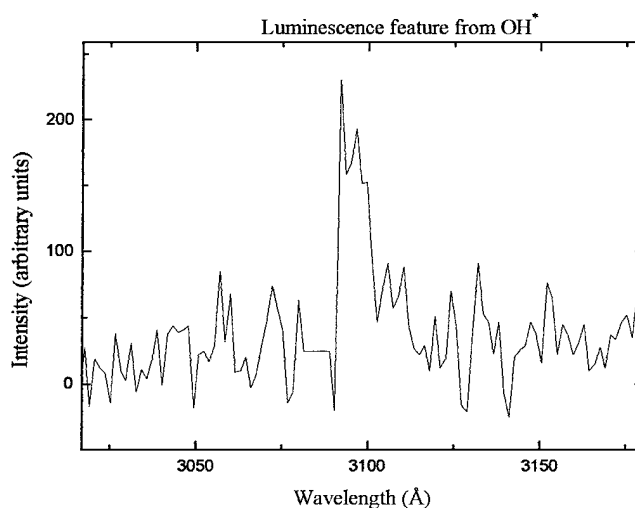


**Figure 40: Luminescence of ice in the UV, showing a line at  $\sim 3060$  Å that is attributed to sputtered  $\text{OH}^*$  excited molecules [Prince et al., 1976].**

A possibility is that water ice luminescence results only around voids and defects within the matrix. The micro-capillary doser we used for film growth is known to create very uniform, low-porosity films, even in the amorphous ice temperature range [Westley et al., 1998]. To grow more porous films, we tried varying the angle of the target with respect to the doser during film growth. Once again, we detected no broad luminescence. Finally, we resorted to growing a film on 5 K substrate by saturating the chamber with water vapor, thus allowing molecules to condense at all angles of incidence. These conditions are known to produce very porous ice. In this experiment, we did not even move the doser up to the target. The film grew just as frost would on a car windshield. The frost yielded no broad luminescence.

Our apparatus should have been sufficient to detect the luminescence seen by other researchers. Since there did not seem to be any experimental oversights in our methods, we wonder whether luminescence in water ice was due to impurities that we were unable to duplicate.

## APPENDIX B - Equipment Calibration

Knowing that the wavelength dispersion from the grating was not linear, we used an Oriel Kr calibration lamp with known emission lines in the visible to plot wavelength against pixel position on the CCD. First, we chose a group of prominent peaks in the lamp's spectra, all of which would fit into one CCD exposure. Next, we tuned the wavelength selector on the spectrometer to the wavelength of one of these peaks. After taking an exposure with the CCD, plotted the spectrum as a function of pixel position, and fit the data with a second order polynomial. The resulting equation was used in all of our subsequent data analysis. Each time we acquired spectra at a new wavelength, we simply changed the polynomial's constant term to match the wavelength we had selected with the spectrometer. When we switched experiments to the ultraviolet range, we performed an identical calibration using a Hg(Ar) test lamp with the other 1200 lpi diffraction grating.

Lamp type	Emission line (Å)
Hg(Ar)	2537
Hg(Ar)	2654
Hg(Ar)	2848
Hg(Ar)	2947
Hg(Ar)	2967
Hg(Ar)	3208
Hg(Ar)	3452
Hg(Ar)	3655
Kr	5570
Kr	5871
Kr	7587
Kr	7602
Kr	7685
Kr	7695

**Table 2: Spectral calibration lines.**

The following are the two calibration equations we used to convert pixel position to wavelength:

- Ultraviolet range:  $X = 352.44545 + 0.68737 \cdot \text{pixel} + 6.32576 \times 10^{-5} \cdot \text{pixel}^2$
- Visible range:  $X = 745.34 + 1.38087 \cdot \text{pixel} + 4.714 \times 10^{-5} \cdot \text{pixel}^2$

In both equations,  $X$  refers to the wavelength dialed in the spectrometer's selector window.

**REFERENCES**

- Baragiola, R.A., and D.A. Bahr, Laboratory studies of the optical properties and stability of oxygen on Ganymede, *Journal of Geophysical Research*, Vol. 103, 25,865-25,872, 1998.
- Brown, W.L., L.J. Lanzerotti, J.M. Poate, and W.M. Augustyniak, "Sputtering" of ice by MeV light ions, *Physical Review Letters*, Vol. 40, 15, 1027-1030, 1978.
- Calvin, W.M., R.E. Johnson, J.R. Spencer, O<sub>2</sub> on Ganymede: spectral characteristics and plasma formation mechanisms, *Geophys. Res. Letts.*, 23, 679-686, 1996.
- Calvin, W.M., and J.R. Spencer, Latitudinal distribution of O<sub>2</sub> on Ganymede: observations with the Hubble Space Telescope, *Icarus*, 130, 505-516, 1997.
- Gerkaines, P.A., W.A. Schutte, and P. Ehrenfreund, Ultraviolet processing of interstellar ice analogs, *Astron. Astrophys.*, 312, 289-305, 1996.
- Hendrix, A.R., C.A. Barth, and C.W. Hord, Ganymede's ozone-like absorber: observations by the Galileo ultraviolet spectrometer, *to be published*.
- Ip, W.-H., D. J. Williams, R. W. McEntire and B. Mauk, Energetic ion sputtering effects at Ganymede, *Geophys. Res. Lett.*, 24, 2631-4, 1997.
- Johnson, R.E., and T.I. Quickenden, Photolysis and radiolysis of water ice on outer solar system bodies, *Journal of Geophysical Research*, Vol. 102, 10,985-10,996, 1997.
- Johnson, R.E., and W.A. Jesser, O<sub>2</sub>/O<sub>3</sub> microatmospheres in the surface of Ganymede, *Astrophys. J.*, 480, L79-L82, 1997.
- Laufer, D., E. Kochavi and A. Bar-Nun, Structure and dynamics of amorphous water ice, *Phys. Rev.*, B36, 9219-9227, 1987.
- McCord, T.B., R.W. Carlson, W.D. Smythe, G.B. Hansen, R.N. Clark, C.A. Hibbitts, F.P. Fanale, J.C. Granahan, M. Segura, D.L. Matson, T.V. Johnson, and P.D. Martin, Organics and other molecules in the surfaces of Callisto and Ganymede, *Science*, 278, 271-275, 1997.
- Merkel, P.B. and W.H. Hamill, Luminescence from thin solid films at 77° K under low-energy electron bombardment, *The Journal of Chemical Physics*, Vol. 54, 4, 1695-1701, 1971.
- Noll, K.S., R.E. Johnson, A.L. Lane, D.L. Domingue and H.A. Weaver, Detection of ozone on Ganymede, *Science*, 273, 341-343, 1996.
- Noll, K.S., T.L. Roush, D.P. Cruikshank, R.E. Johnson, and Y.J. Pendleton, Detection of ozone on Saturn's satellites Rhea and Dione, *Nature*, 388, 45-47, 1997.
- Okabe, H., *Photochemistry of Small Molecules*, John Wiley & Sons, 1978.



- Orton, G.S., J.R. Spencer, L.D. Travis, T.Z. Martin and L.K. Tamppari, Galileo photopolarimeter-radiometer observations of Jupiter and the Galilean satellites, *Science*, 274, 389-391, 1996.
- Prince, R.H., G.N. Sears and F.J. Morgan, Fluorescence of ice by low energy electrons, *The Journal of Chemical Physics*, vol. 64, 10, 3978-3985, 1976.
- Sack, N. J., and R. A. Baragiola, Sublimation of vapor-deposited water ice below 170 K, and its dependence on growth conditions, *Phys. Rev.*, B48, 9973-9978, 1993.
- Schumb, W.C., C.N. Satterfield, and R.L. Wentworth, *Hydrogen Peroxide*, Reinhold Publishing Corp., 1955.
- Sedlacek, A.J. and C.A. Wight, Photochemistry of solid ozone, *J. Phys. Chem.*, 93, 509-511, 1989.
- Siegel, M.W., Cross sections for production of  $O_3^+$ ,  $O_2^+$ , and  $O^+$  by electron impact ionization of ozone between threshold and 100 eV., *Intl Journal of Mass Spectrometry and Ion Phys*, 44, 19-36, 1982.
- Spencer, J.R., Thermal segregation of water ice on the Galilean satellites, *Icarus*, 69, 297-313, 1987.
- Spencer, J.R., W. M. Calvin, and M. J. Person, Charge-coupled device spectra of the Galilean satellites: Molecular oxygen on Ganymede, *J. Geophys. Res.*, 100, 19,049-19,056, 1995.
- Spencer J.R., Upper limits for condensed  $O_2$  on Saturn's icy satellites and rings, *Icarus* (in press).
- Strazzula, G.; G.A. Baratta, G. Leto, and G. Foti, Ion-beam induced amorphization of crystalline water ice, *Europhys. Lett.* 18, 517-22, 1992.
- Vidal, R.A., D. Bahr, R.A. Baragiola, and M. Peters, Oxygen on Ganymede: Laboratory studies, *Science*, 276, 1839-1842, 1997.
- Westley, M.S., *Vapor Deposited Water Ice: Structural Properties, Effects of Ultraviolet Light, and Astrophysical Implications*, Master of Science Thesis, Univ. of Virginia, 1994.
- Westley, M.S., G.A. Baratta and R.A. Baragiola, Density, porosity and index of refraction of ice films formed by vapor deposition at low-temperatures, *J. Chem. Phys.*, 108, 3321-3326, 1998.